Characterization and Modeling of Dual-Single-Layer PCB Resonators for Megahertz Hybrid Inductive and Capacitive Wireless Power Transfer

Kerui Li, *Member, IEEE*, Jiayang Wu, *Member, IEEE*, Siew-Chong Tan, *Fellow, IEEE*, Ka Wai Eric Cheng, *Fellow, IEEE*, and Shu-Yuen Ron Hui, *Fellow, IEEE*

***Abstract*—Recent advancements in the dual-single-layer printed-circuit-board (DSL-PCB) resonators open a door to designing megahertz (MHz) wireless power transfer (WPT) systems characterized by high-quality factor, energy efficiency, and suitability for mass production. This article introduces a novel procedure to characterize the DSL-PCB resonator structure and derive the parameters for an equivalent circuit model capable of addressing both capacitive and inductive WPT for a wide-frequency range. The proposed DSL-PCB resonator circuit model is practically evaluated using various dielectric materials in the gap between the two single-layer PCBs. Then, two resonator models are used to form the transmitter and receiver resonators in a hybrid inductive and capacitive WPT system. A new mathematical proof is included to confirm that the coupling coefficient of hybrid WPT is always higher than those of the inductive WPT and capacitive WPT. Theoretical predictions and experimental validations of the system are conducted within the MHz frequency range. The predicted performance characteristics of the WPT system based on DSL-PCB resonators align closely with experimental measurements. The proposed resonator model, along with its corresponding WPT framework, establishes a solid theoretical foundation for future research into MHz WPT systems leveraging DSL-PCB resonators.**

***Index Terms*—Capacitive power transfer (CPT), hybrid wireless power transfer (WPT), inductive power transfer (IPT), printed-circuit-board (PCB) resonators.**

I. Introduction

With the revival of modern wireless power transfer (WPT) research and developments in the 1990s and early 2000s [2], [3], [4], [5], [6] and the establishment of the Qi wireless charging standard launched by the Wireless Power Consortium (WPC) [7] in 2010, the WPT market has grown to USD 22.17 billion in 2022 and is projected to grow to USD 129 billion by 2023 according to Fortune Business Insights [8] in the sectors of consumer electronics, automotive, industrial, healthcare, aerospace, and defense. Hui et al. [9], [10] point out that Tesla's early patents, such as [11], have visually pointed to the use of magnetic resonance and high-quality factor requirement for high energy efficiency in WPT. In general, the energy efficiency of a WPT system is proportional to the product of k and Q, where k is the coupling coefficient of the transmitter and receiver coil resonators and Q is the quality factor of the coil resonator [9]. Fig. 1 shows the existing power profile of WPT applications [12] based on the wireless charging standards of the Society for Automobile Engineers, WPC, and Airfuel Alliance. It is noted that there is an uncharted territory at the high-frequency (MHz) and high-power region. There are individual reports on attempts to operate WPT systems at the megahertz (MHz) range. On the one hand, some researchers have pioneered various forms of discrete inductors for MHz operation [13], [14], [15], [16]. On the other hand, other researchers have investigated printed-circuit-board (PCB) resonators for WPT applications [17], [18], [19]. Compared with kilohertz WPT systems, these MHz WPT systems generally feature high transmission efficiency because of an improved kQ factor, small size, and high manufacturing precision because of PCB manufacturing techniques [12].

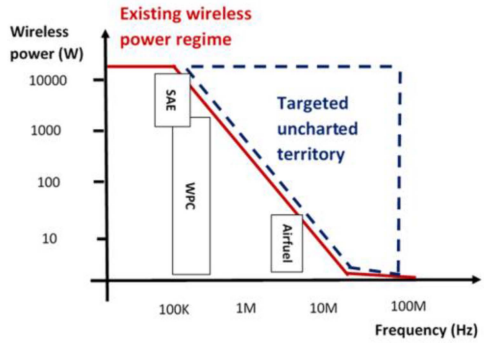

Fig. 1. Power profile of existing WPT applications [12] (IEEE copyright).

A traditional PCB resonator for WPT application has copper coils printed on the "two sides" of the same PCB board

Received 21 March 2025; revised 19 May 2025; accepted 9 June 2025. Date of publication 16 June 2025; date of current version 5 August 2025. This work was supported by the Hong Kong Research Council through Theme-Based Research Project under Grant T23-708/24-N. Recommended for publication by Associate Editor J. Biela. *(Corresponding author: Shu-Yuen Ron Hui.)*

Kerui Li, Jiayang Wu, and Siew-Chong Tan are with the Department of Electrical Engineering, City University of Hong Kong, Hong Kong SAR, China (e-mail: keruili@cityu.edu.hk; jiayang.wu@cityu.edu.hk; siewctan@cityu.edu.hk).

Ka Wai Eric Cheng is with the Department of Electrical Engineering and Computer Science, University of California, Merced, CA 95343 USA (e-mail: ericcheng@ucmerced.edu).

Shu-Yuen Ron Hui is with the Department of Electrical Engineering, City University of Hong Kong, Hong Kong SAR, China, and also with the Department of Electrical and Electronic Engineering, Imperial College London, SW7 2BX London, U.K. (e-mail: eeronhui@cityu.edu.hk).

Color versions of one or more figures in this article are available at https://doi.org/10.1109/TPEL.2025.3580073.

Digital Object Identifier 10.1109/TPEL.2025.3580073

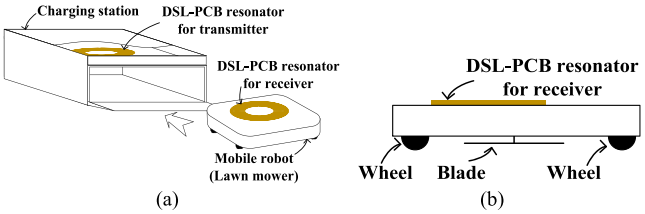

Fig. 2. Potential applications [31]. (a) Wireless charging/docking station for lawn mowers. (b) Side view of the lawn mower.

and is, therefore, referred as a two-layer or double-layer PCB (DL-PCB) resonator [19]. At an operating frequency below the MHz range, such DL-PCB resonators work very well as demonstrated in the wireless power domino system [19]. However, it was pointed out in [20] and [21] that the dielectric power loss in the PCB materials enclosed by two printed coils could be significant at MHz operation.

In this article, the dual-single-layer printed-circuit-board (DSL-PCB) resonator structure originally reported in [1], [20], and [21] is further investigated for hybrid inductive and capacitive WPT. The additional capacitive coupling relies solely on the near-field electric flux for wireless power transmission, without significantly increasing the conduction current, and therefore results in high transmission efficiency. Moreover, the incorporation of capacitive power transfer (CPT) introduces a parallel transmission path, effectively increasing the overall coupling, transmission efficiency, and power.

DSL-PCB resonators achieve high performance through the synergy of self-resonance and hybrid coupling. Self-resonance alters the current and voltage distribution within the resonator [1], [21], which facilitates a high-Q resonance and reshapes the electric and magnetic fields to enhance coupling. The conventional circuit models for inductive couplers [22], [23], capacitive couplers [24], [25], and hybrid couplers [26], [27], [28] are insufficient for analyzing this structure because they overlook the synergistic effects of self-resonance and hybrid coupling. Notably, Wang et al. [29], [30] present a similar resonator structure, published after our conference publication [1]. Their models oversimplify the combined effects. Alternative, 3-D finite-element modeling could provide the accurate results, but its high computational cost and incompatibility with circuit simulator make it less practical for system studies. The proposed equivalent circuit model enables both time-domain and frequency-domain analysis of the resonator and the WPT system. Moreover, the equivalent circuit model allows for cosimulation with power electronics' circuits and control, facilitating system-level integration and optimization.

The DSL-PCB resonators can be used for charging mobile robots, such as electric lawn mowers [31]. As shown in Fig. 2(a), the lawn mowers are charged inside the charging/docking station with a roof-top wireless charger. Traditional wireless chargers with the transmitter on the ground do not suit this application because there are metallic blades in the bottom structure of the electric lawn mowers, as shown in Fig. 2(b). Charging mobile robots from the top can minimize the distance between the transmitter and receiver (potentially reduce to millimeter level) to achieve higher transmission efficiency. This paper is an extension of a previous conference publication [1].

TABLE I
PHYSICAL PARAMETERS OF THE SPIRAL WINDINGS

	Winding 1	Winding 2
First turn trace width	13.008 mm	15.997 mm
Radius of outermost trace	100 mm	99 mm
Radius of innermost trace	29.57 mm	55.110 mm
Ratio of adjacent trace width	0.963	1.096
Number of turns	5	2
Distance between adjacent turns	2.437 mm	3.476 mm
Copper thickness	2 oz (~ 65 μm)	2 oz (~ 65 μm)

The bold entities are the headings of the rows and columns.

To summarize, the novel contributions include the following:

1) an equivalent circuit model of the DSL-PCB resonator for *both* capacitive and inductive WPT;
2) a parameter extraction procedure for such resonator model;
3) a model of two coupled DSL-PCB resonators for use as a WPT system;
4) practical verification of the DSL-PCB resonator model;
5) practical verification of the WPT system model based on the DSL-PCB resonators;
6) proof that hybrid coupling is stronger than both capacitive and inductive coupling;
7) enhanced kQ factor and optimal transmission efficiency for a pair of coupled DSL-PCB resonators;
8) improved Pareto fronts that optimize the tradeoffs between transmission efficiency and power.

II. DSL-PCB Resonator Structures With Hybrid Inductive Power Transfer (IPT) and CPT Capability

Fig. 3(a) shows the general structure of the DSL-PCB resonator with hybrid IPT and CPT capability. As an example, it may consist of two asymmetric printed spiral windings, as shown in Fig. 3(b) and (c). Note that the coil is printed on "one side" of a PCB. These two single-layer PCB coils (separated with a middle layer that can be an airgap with no dielectric loss or a dielectric material with very low-loss tangent) form one resonator. For this reason, this structure is named DSL-PCB resonator.

When one of the PCB windings is electrically excited in an ac manner, an ac electromagnetic field is generated within the region between the two spiral windings of each DSL-PCB resonator. This phenomenon can be represented as a resonator tank with distributed inductance and capacitance. The windings are designed with the aid of finite-element simulation. The flowchart is shown in Fig. 3(d). In this example, there are five turns for winding-1 and two turns for winding-2. The dimensions of the PCB boards are 200 mm × 200 mm. The specific physical parameters of these two windings are shown in Table I. It should be noted that these two spiral windings, as shown in Fig. 3(b) and (c), differ in their conductor areas. The overlapped conductor

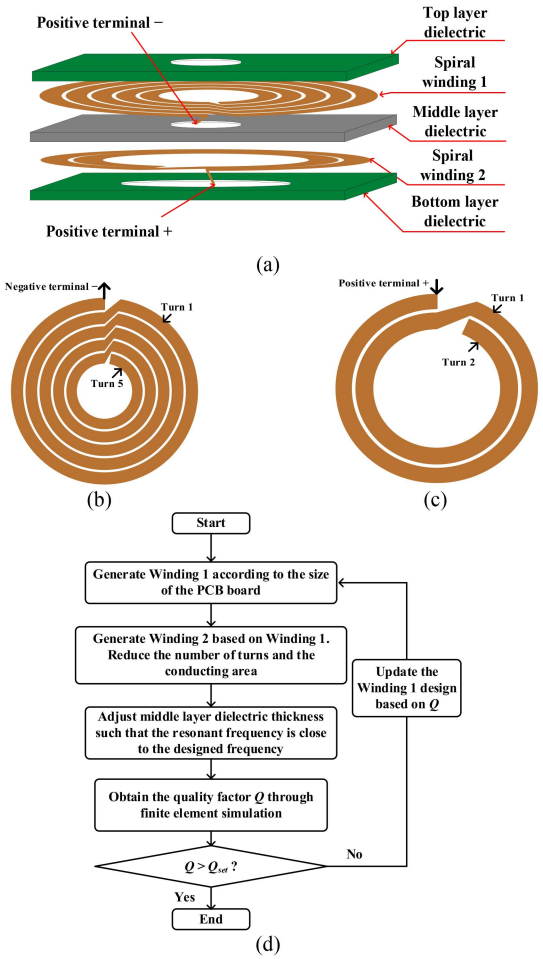

Fig. 3. General structure of the DSL-PCB resonator with hybrid IPT and CPT capability. (a) Physical structure. (b) Spiral winding 1. (c) Spiral winding 2. (The conductor area of spiral winding 1 is larger than that of spiral winding 2 in this example.) (d) Design flowchart of the spiral windings.

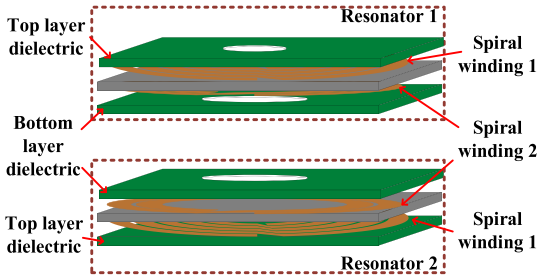

Fig. 4. Pair of DSL-PCB resonators forming the transmitter and receiver resonators in WPT system [1], [20].

area contributes to self-capacitance, while the nonoverlapped conductor area enables mutual capacitive coupling with another DSL-PCB resonator.

Two DRL-PCB resonators can be used to form the transmitter and receiver resonators in a WPT system, as shown in Fig. 4. To enable hybrid inductive and capacitive coupling, the bottom layers (winding-2) of the transmitter and receiver resonators are positioned face-to-face. This arrangement allows both the

TABLE II
COMPARISON OF DIELECTRIC MATERIALS

Material	FR-4	Mica	Air
Nominal dielectric constant	3.8–4.8	3–6	1
Measured dielectric constant*	5.07	1.30	1
Typical loss tangent	0.02	0.0003	~0

*The dielectric constant is measured by comparing the capacitance of a capacitor filled with a dielectric material to the capacitance of an identical capacitor filled with air as its dielectric.
The bold entities are the headings of the rows and columns.

TABLE III
PHYSICAL PARAMETERS OF THREE RESONATOR DESIGNS

		Design 1	Design 2	Design 3
Top layer dielectric	Material	FR-4	FR-4	Air
	Thickness	1.6 mm	1.6 mm	N.A.
Middle layer dielectric	Material	Air	Mica	FR-4
	Thickness	1.6 mm	1.6 mm	1.6 mm
Bottom layer dielectric	Material	FR-4	FR-4	Air
	Thickness	1.6 mm	1.6 mm	N.A.

The bold entities are the headings of the rows and columns.

electric and magnetic flux generated by the electrically excited spiral windings to be directly coupled between the resonators. If the resonators were not placed in this orientation, the magnetic flux coupling would remain unchanged. But the electric flux generated by spiral winding-2 of one resonator is canceled out by the electric flux from the spiral winding-1 of another resonator, thereby weakening capacitive coupling between the resonators.

The main self-capacitance of the resonator arises from the electric field between the copper traces. The main electric flux predominantly flows across the middle dielectric layer (e.g., a layer of air or mica). A small amount of fringing electric flux between adjacent copper traces can be represented as intrawinding capacitance. The self-capacitance is also affected by dielectric materials. For comparison, FR4, mica, and air are selected as the middle dielectric layers. The key properties of these materials are shown in Table II. The mica sheets used in Design 2 exhibit a measured dielectric constant of only 1.3, lower than their nominal value. The mica sheets used in this test may contain some impurities.

Fig. 5(a)–(c) shows three different implementations based on the general DSL-PCB resonator structure. For the first design, as shown in Fig. 5(a), the top and bottom layer dielectrics are FR-4 PCB substrates, while the middle layer dielectric is air. For the second design, as shown in Fig. 5(b), the top and bottom layer dielectrics are FR-4 PCB substrates, while the middle layer dielectric is mica. For the third design, as shown in Fig. 5(c), the top and bottom layer dielectrics are air, while the middle layer dielectric is FR-4 (i.e., a traditional DL-PCB resonator structure). The specific design parameters of these three resonators are listed in Table III.

III. ACCURATE MODELS FOR THE PCB RESONATORS

A. Circuit Model and Parameter Extraction of the Standalone DSL-PCB Resonator

1) Magnetic and Electric Flux Distribution of the Standalone DSL-PCB Resonator: Given the similar properties of these three

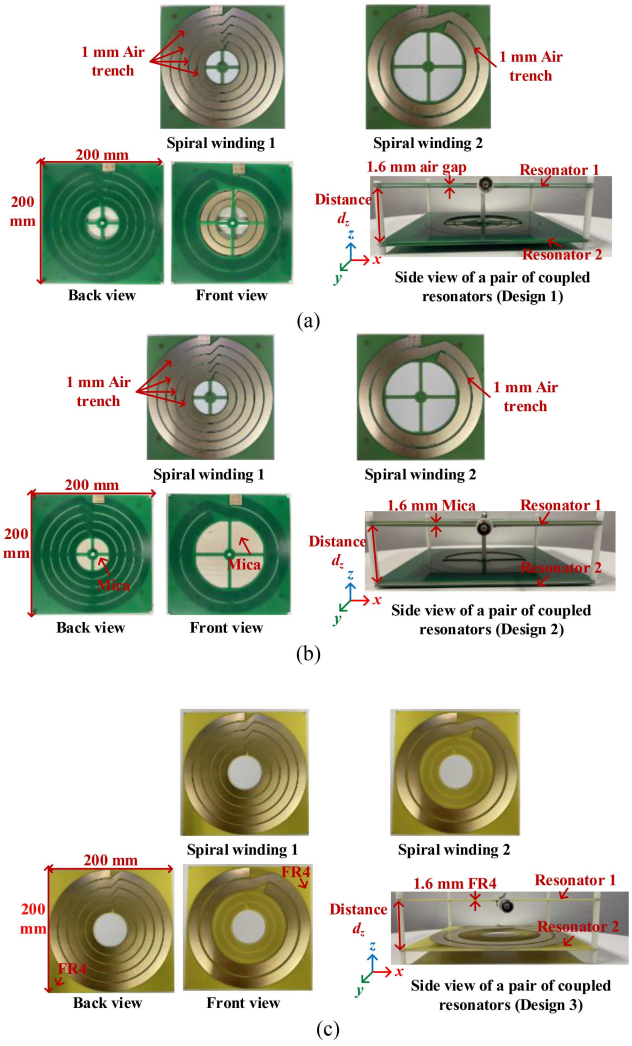

Fig. 5. Three different implementations based on the general PCB resonator structure. (a) Design 1. (b) Design 2. (c) Design 3.

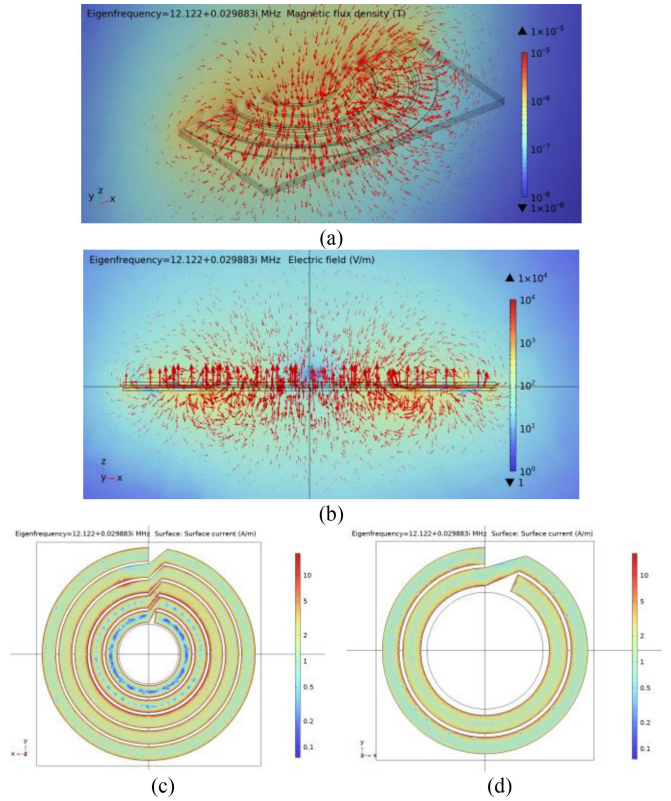

Fig. 6. Finite-element simulation results of the resonator at eigenfrequency. (a) Magnetic flux distribution. (b) Electric flux distribution. (c) and (d) Surface current distribution of spiral windings 1 and 2.

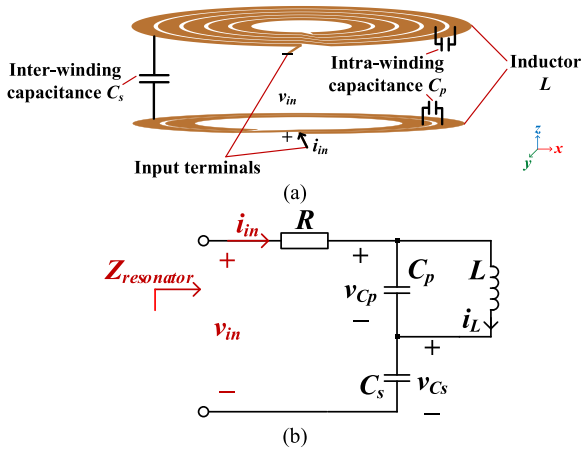

Fig. 7. Equivalent circuit model and its correspondence to the physical structure of a standalone DSL-PCB resonator. (a) Model-structure correspondence (dielectric layers are hidden). (b) Circuit model.

designs, Design 1 is selected as an example to perform the magnetic and electric flux analysis. This analysis will provide heuristic to derive the corresponding circuit model. The finite-element simulation is performed using eigenmode. The resulting eigenfrequency of the resonator is $12.122 + i2.988\times10^{-2}$ MHz. Fig. 6(a)–(d) shows the magnetic flux, electric flux, and surface current distributions on spiral windings 1 and 2, respectively.

2) Circuit Model of a DSL-PCB Resonator: Fig. 7(a) shows the equivalent circuit model derived from the physical structure of DSL-PCB resonator. The dielectric layers are hidden to better illustrate how the equivalent circuit model is constructed. Windings 1 and 2 are corresponding to the main inductor L. The middle dielectric layer contributes to the interwinding capacitance C_s. The stray capacitance between adjacent turns of the spiral windings contributes to the intrawinding capacitance C_p, which is in parallel with L.

Fig. 7(b) shows the equivalent circuit model for a standalone DSL-PCB resonator. From the finite-element analysis, as shown in Fig. 6, the main magnetic flux is observed to concentrate at the center of the resonator, while the main electric flux concentrates between the two copper spiral windings. These magnetic and electric fluxes will contribute to the main inductor L and the interwinding capacitance C_s. In addition, some electric flux is observed between the adjacent turns of the spiral windings, which results in the intrawinding capacitance C_p. The conducting area of spiral windings is sufficiently utilized, suggesting a relatively

low conduction loss resistance R. In the central area of spiral winding 1 [see Fig. 6(c)], the current decreases significantly due to self-resonance. This challenges the assumptions of consistent current distribution used in inductor modeling [22], [23]. As a result, the magnetic field and inductive coupling of DSL-PCB resonator cannot be accurately characterized by conventional inductor models.

The state-space model of the standalone DSL-PCB resonator, with ac input voltage v_{in} as source and ac current i_{in} as output variable, can be written as

$$\begin{bmatrix} \frac{di_L(t)}{dt} \\ \frac{dv_{Cs}(t)}{dt} \\ \frac{dv_{Cp}(t)}{dt} \end{bmatrix} = \begin{bmatrix} 0 & 0 & \frac{1}{L} \\ 0 & -\frac{1}{RC_s} & -\frac{1}{RC_s} \\ -\frac{1}{C_p} & -\frac{1}{RC_p} & -\frac{1}{RC_p} \end{bmatrix} \begin{bmatrix} i_L(t) \\ v_{Cs}(t) \\ v_{Cp}(t) \end{bmatrix} + \begin{bmatrix} 0 \\ \frac{1}{RC_s} \\ \frac{1}{RC_p} \end{bmatrix} v_{\text{in}}(t);$$

$$i_{\text{in}}(t) = \begin{bmatrix} 0 & -\frac{1}{R} & -\frac{1}{R} \end{bmatrix} \begin{bmatrix} i_L(t) \\ v_{Cs}(t) \\ v_{Cp}(t) \end{bmatrix} + \frac{1}{R} v_{\text{in}}(t). \quad (1)$$

The self-resonant frequency f_r and quality factor $Q_{\text{resonator}}$ of the resonator are derived from the state matrix of (1) using the eigenvalues λ [32], [33]

$$f_r = \frac{|\lambda|}{2\pi}; \quad (2)$$

$$Q_{\text{resonator}} = \left| \frac{\text{imag}(\lambda)}{2 \times \text{real}(\lambda)} \right|. \quad (3)$$

where imag(λ) and real(λ) are the imaginary and real parts of λ, respectively. The complex resonant angular frequency of the model $\omega_c = i\lambda$ [33]. For modeling a high-Q resonator, real(λ) is much smaller than imag(λ), and, hence, the resonant frequency can also be approximated as $f_r \approx |\frac{\text{imag}(\lambda)}{2\pi}|$.

3) New Circuit Parameter Extraction Procedure: The circuit parameters can be extracted using the measured input impedance of the resonator $Z_{\text{resonator}}$ (i.e., $Z_{\text{resonator}}(\omega) = \frac{v_{\text{in}}(\omega)}{i_{\text{in}}(\omega)}$) and quality factor $Q_{\text{resonator}}$. The data for the input impedance $Z_{\text{resonator\_data}}$ of the standalone resonator at different frequencies are measured using a network analyzer. The data for the quality factor of the resonator $Q_{\text{resonator\_data}}$ are obtained by measuring the 3-dB bandwidth of $Z_{\text{resonator\_data}}$. The theoretical frequency response $Z_{\text{resonator}}(\omega)$ is derived from the state-space model (1). Over a wide-frequency range, the reactive components show much higher impedance than the resistance R, and hence, the traditional curve fitting method used in [21] is not suitable to extract the accurate resistance R. As a result, we proposed to use a two-step approach to extract the parameters.

In the first step, the reactive components (i.e., C_s, C_p, and L) are characterized using $Z_{\text{resonator\_data}}$ as

$$\hat{L}, \widehat{C_s}, \widehat{C_p} = \underset{L,R,C_s,C_p}{\text{argmin}} \; ||20\log_{10}|Z_{\text{resonator}}| - 20\log_{10}|Z_{\text{resonator\_data}}||_2 \quad (4)$$

where the hat notation ^ represents the adopted estimated value, the operator $|\cdot|$ represents the amplitude of the complex impedance, and the operator $\|\cdot\|_2$ represents the Euclidean norm. The resulting C_s, C_p, and L are finalized after solving the optimization problem (4). The first step is consistent with the curve fitting method outlined in [21].

In the second step, the resulting parameters $\widehat{C_s}$, $\widehat{C_p}$, and $\hat{L}$ will be substituted into the state-space model and used to derive the quality factor $Q_{\text{resonator}}$ based on (3). The final value of R is obtained by minimizing the difference between $Q_{\text{resonator}}$ and the measured quality factor $Q_{\text{resonator\_data}}$

$$\hat{R} = \underset{R}{\arg\min} \left\| Q_{\text{resonator}}\left(L = \hat{L},\ C_s = \widehat{C_s},\ C_p = \widehat{C_p}\right) - |Q_{\text{resonator\_data}}| \right\|_2. \quad (5)$$

It is worth noting that the estimated R obtained from (4) can be used as the initial searching value to expedite solving the optimization problem (5).

B. Circuit Model and Parameter Extraction of the Coupled DSL-PCB Resonators

1) Magnetic and Electric Flux Distribution of the Coupled DSL-PCB Resonators: The finite-element simulation of a pair of coupled DSL-PCB resonators, with 10-mm distance along the z-axis and 100-Ω load resistance, is performed using eigenmode. The resulting eigenfrequency of the resonator is 10.005 + i1.1341 MHz. Fig. 8(a)–(c) shows the magnetic flux, electric flux, and displacement current density of these two coupled DSL-PCB resonators, respectively.

2) Circuit Model of the Coupled DSL-PCB Resonators: Fig. 9(a) shows the equivalent circuit model derived from the physical structure of coupled DSL-PCB resonators. The dielectric layers are hidden to better illustrate how the equivalent circuit model is constructed. The magnetic flux is observed to pass through and link both resonators, which can be represented by a mutual inductance M in the equivalent circuit model. Stray capacitance between the outer windings constitutes one part of the mutual capacitance C_m; stray capacitance between the inner windings constitutes the remaining part.

Fig. 9(b) shows the equivalent circuit model for a pair of coupled DSL-PCB resonators. Based on the finite-element analysis, as shown in Fig. 8, both electric and magnetic fluxes are utilized for coupling between the resonators. The magnetic flux is observed to pass through and link both resonators, which can be represented by a mutual inductance M in the equivalent circuit model. In addition, electric flux is observed between the two resonators, as represented by the mutual capacitance C_m in the circuit model. Furthermore, as a portion of displacement current penetrates the PCB substrate through mutual electric flux, a series resistance R_m is included in the circuit model to account for the dielectric loss caused by this electric coupling.

Finally, the electric flux also affects the intrawinding capacitance C_p and interwinding capacitances C_s of the individual

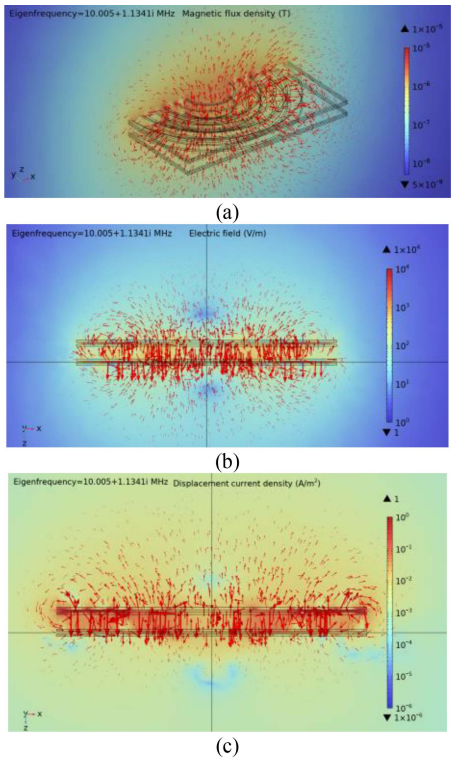

Fig. 8. Finite-element simulation results of a pair of coupled resonators at eigenfrequency. (a) Magnetic flux distribution. (b) Electric flux distribution. (c) Displacement current density.

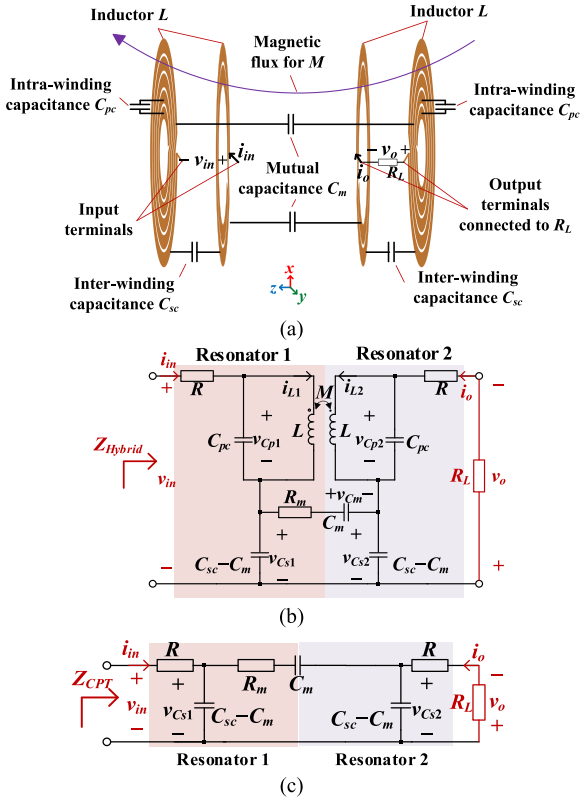

Fig. 9. Physical WPT system structure based on a pair of coupled DSL-PCB resonators and its equivalent circuit model. (a) WPT system structure (dielectric layers are hidden). (b) Full-order model. (c) Reduced-order model and the resulting CPT system at low operating frequency.

resonators, and they are represented by C_{pc} and C_{sc}, respectively, in the circuit model of coupled resonators.

The full-order circuit model of these coupled DSL-PCB resonators as a WPT system is shown in Fig. 9(b). A low-frequency (reduced-order) equivalent model, as shown in Fig. 9(c), can be derived from the full-order model by assuming that the reactance of the self-inductance L in the low-frequency range is almost zero, i.e., $\lim_{\omega\to 0}\omega L = 0$, allowing it to be short circuited at low operating frequency. The low-frequency equivalent model is a typical CPT system.

This model illustrates the nature of the hybrid coupling mechanism. At low frequencies, the electric flux dominates the coupling between the resonators (i.e., C_m). However, as the frequency increases, the magnetic flux introduced by the electrically excited spiral windings (i.e., M) pronounces, realizing the hybrid capacitive and inductive coupling between the two DSL-PCB resonators.

The full-order model of the coupled PCB resonators, with ac input voltage v_{in} as source and ac current i_{in} and i_o as output variable, can be represented as (6) shown at the bottom the next page,where $\boldsymbol{L_{matrix}} = \begin{bmatrix} L & M \\ M & L \end{bmatrix}$, $\boldsymbol{C_{s\_matrix}} = \begin{bmatrix} C_{sc}-C_m & C_m & 0 \\ 0 & C_m & 0 \\ 0 & -C_m & C_{sc}-C_m \end{bmatrix}$, $\boldsymbol{C_{p\_matrix}} = \begin{bmatrix} C_{pc} & 0 \\ 0 & C_{pc} \end{bmatrix}$, $\boldsymbol{Y_{matrix1}} = \begin{bmatrix} -1/R & 0 & 0 \\ 1/R_m & -1/R_m & -1/R_m \\ 0 & 0 & -1/(R_L+R) \end{bmatrix}$, $\boldsymbol{Y_{matrix2}} = \begin{bmatrix} -1/R & 0 \\ 0 & 0 \\ 0 & -1/(R_L+R) \end{bmatrix}$, $\boldsymbol{Y_{matrix3}} = \begin{bmatrix} -1/R & 0 \\ 0 & -1/(R_L+R) \end{bmatrix}$, $\mathbf{Y_{matrix4}} = [1/R, 0, 0]^{\mathrm{T}}$, $\mathbf{Y_{matrix5}} = [1/R, 0]^{\mathrm{T}}$, $\mathbf{i_{L\cdot matrix}} = [i_{L1}(t), i_{L2}(t)]^{\mathrm{T}}$, $\mathbf{v_{s\cdot matrix}} = [v_{Cs1}(t), v_{Cm}(t), v_{Cs2}(t)]^{\mathrm{T}}$, $\mathbf{v_{p\cdot matrix}} = [v_{Cp1}(t), v_{Cp2}(t)]^{\mathrm{T}}$, and $\mathbf{0}$ is the zero matrix.

Similarly, the reduced-order model, which can be derived from the full-order model by eliminating $\boldsymbol{i_{L\cdot matrix}}$ and $\boldsymbol{v_{p\cdot matrix}}$, is expressed as

$$\begin{aligned} \frac{d\boldsymbol{v_{s\_matrix}}}{dt} &= \boldsymbol{C_{s\_matrix}}^{-1}\boldsymbol{Y_{matrix1}}\boldsymbol{v_{s\_matrix}} \\ &\quad + \boldsymbol{C_{s\_matrix}}^{-1}\boldsymbol{Y_{matrix4}}v_{\text{in}}; \\ \begin{bmatrix} i_{\text{in}} \\ i_o \end{bmatrix} &= \boldsymbol{Y_{matrix2}}^{\mathrm{T}}\boldsymbol{v_{p\_matrix}} + \boldsymbol{Y_{matrix5}}v_{\text{in}}. \end{aligned} \tag{7}$$

The frequency response of the input impedance of the coupled resonators $Z_{\text{Hybrid}}(\omega)$ and $Z_{\text{CPT}}(\omega)$ can be derived from the state-space models in (6) and (7), respectively.

3) Circuit Parameter Extraction: The circuit parameters of the coupled resonators are extracted using the input impedance of the coupled resonators. Since the coupling mechanism involves both electric and magnetic flux, extracting both the mutual capacitance C_m and mutual inductance M concurrently

using the impedance Z_{Hybrid} may lead to significant discrepancies and convergence issues. To address this issue, a successive data-fitting approach is employed to extract these parameters separately.

At the low-frequency region, inductive coupling is negligible. The self- and mutual capacitances C_{sc}, C_{pc}, and C_M can be independently extracted based on the reduced-order model. Once mutual capacitances are extracted, mutual inductance M can be independently determined based on the full-order model. Consequently, the parameter extraction process involves two successive steps.

The first step is to use the low-frequency (e.g., from $0.05f_r$ to $0.15f_r$) impedance data for extracting the capacitance C_{sc}, C_{pc}, and C_M. To further improve the accuracy, both impedance data with an open-circuit load (i.e., $R_L = +\infty$), denoted as $Z_{\text{CPT·OC·data}}$, and a short-circuit load (i.e., $R_L = 0$), denoted as $Z_{\text{CPT·SC·data}}$, are utilized. The impedance data at different frequencies are measured using the network analyzer

$$\begin{aligned}\widehat{C_{pc}}, \widehat{C_{sc}}, \widehat{C_M} = \underset{C_{pc},C_{sc},C_M}{\text{argmin}} \; & \Big|\Big|20\log_{10}\left|Z_{\text{CPT}}\left(R\right.\right. \\ & \left.\left. = \hat{R},\ R_M = 0,\ R_L = +\infty\right)\right| \\ & - 20\log_{10}\left|Z_{\text{CPT\_OC\_data}}\right|\Big|\Big|_2 \\ & + \Big|\Big|20\log_{10}\left|Z_{\text{CPT}}\left(R = \hat{R},\ R_M = 0,\ R_L = 0\right)\right| \\ & - 20\log_{10}\left|Z_{\text{CPT\_SC\_data}}\right|\Big|\Big|_2. \end{aligned} \tag{8}$$

The second step is to extract the mutual inductance M and the high-frequency resistance associated with the mutual capacitance. Based on the full-range impedance data with an open-circuit load, i.e., $Z_{\text{Hybrid·OC·data}}$, and a short-circuit load, i.e., $Z_{\text{Hybrid·SC·data}}$, these parameters are extracted as follows:

$$\begin{aligned}\widehat{R_M},\ \hat{M} = \underset{R_M,M}{\text{argmin}} \; & \Big|\Big|20\log_{10}\left|Z_{\text{Hybrid}}\left(R = \hat{R},\ L = \hat{L},\ C_{sc}\right.\right. \\ & \left.\left. = \widehat{C_{sc}},\ C_{pc} = \widehat{C_{pc}},\ R_L\right.\right. \\ & \left.\left. = \ +\infty\right)\right| - 20\log_{10}\left|Z_{\text{Hybrid\_OC\_data}}\right|\Big|\Big|_2 \\ & + \Big|\Big|20\log_{10}\left|Z_{\text{Hybrid}}\left(R = \hat{R},\ L = \hat{L},\ C_{sc}\right.\right. \\ & \left.\left. = \widehat{C_{sc}},\ C_{pc} = \widehat{C_{pc}},\ R_L = 0\right)\right| \\ & - 20\log_{10}\left|Z_{\text{Hybrid\_SC\_data}}\right|\Big|\Big|_2. \end{aligned} \tag{9}$$

TABLE IV
CIRCUIT PARAMETERS OF THREE RESONATOR DESIGNS

	Design 1	**Design 2**	**Design 3**
f_r **(MHz)**	11.64	10.50	5.85
$Q_{resonator}$	210.6	177.5	56.2
L **(μH)**	0.989	0.981	1.033
R **(Ω)**	0.649	0.689	1.104
C_s **(pF)**	137.6	170.4	559.8
C_p **(pF)**	51.6	63.8	155.4

The bold entities are the headings of the rows and columns.

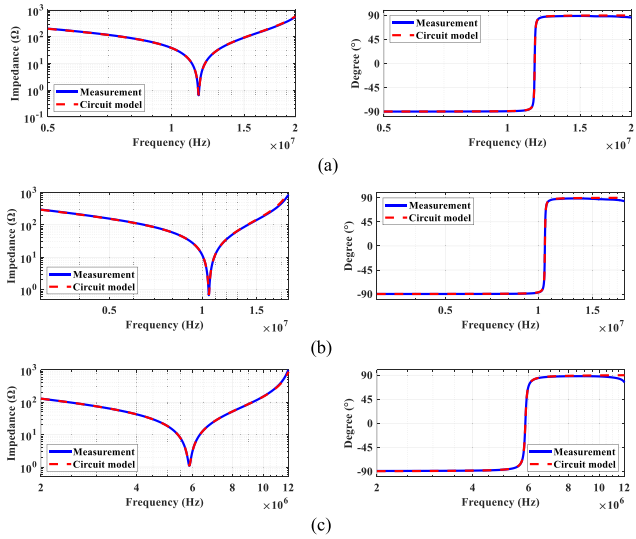

Fig. 10. Input impedance curves of the standalone resonators. Amplitude and phase plots of the input impedance for (a) resonator design 1, (b) resonator design 2, and (c) resonator design 3.

Since the running time is not a primary concern when characterizing the resonators, the optimization problems can be effectively solved using derivative-free methods, without deriving the gradient.

IV. WPT System With Hybrid Inductive and Capacitive Couplings

A. Circuit Parameters of the Standalone Resonators

The circuit parameters of the standalone resonators were extracted using the procedure in Section III and are summarized in Table IV. The input impedance curves of these three designs are shown in Fig. 10. The results obtained from the circuit model and measurements are in good agreement.

$$\begin{aligned}\begin{bmatrix}\frac{d\boldsymbol{i_{L\_matrix}}}{dt}\\ \frac{d\boldsymbol{v_{s\_matrix}}}{dt}\\ \frac{d\boldsymbol{v_{p\_matrix}}}{dt}\end{bmatrix} &= \begin{bmatrix}0 & 0 & \boldsymbol{L_{matrix}}^{-1}\\ 0 & \boldsymbol{C_{s\_matrix}}^{-1}\boldsymbol{Y_{matrix}}1 & \boldsymbol{C_{s\_matrix}}^{-1}\boldsymbol{Y_{matrix}}2\\ -\boldsymbol{C_{p\_matrix}}^{-1} & \boldsymbol{C_{p\_matrix}}^{-1}\boldsymbol{Y_{matrix}}2^{\mathbf{T}} & \boldsymbol{C_{p\_matrix}}^{-1}\boldsymbol{Y_{matrix}}3\end{bmatrix}\begin{bmatrix}\boldsymbol{i_{L\_matrix}}\\ \boldsymbol{v_{s\_matrix}}\\ \boldsymbol{v_{p\_matrix}}\end{bmatrix}\\ &+ \begin{bmatrix}0\\ \boldsymbol{C_{s\_matrix}}^{-1}\boldsymbol{Y_{matrix}}4\\ \boldsymbol{C_{p\_matrix}}^{-1}\boldsymbol{Y_{matrix}}5\end{bmatrix}v_{\text{in}}\begin{bmatrix}i_{\text{in}}\\ i_o\end{bmatrix} = \begin{bmatrix}0 & \boldsymbol{Y_{matrix}}2^{\mathbf{T}} & \boldsymbol{Y_{matrix}}3\end{bmatrix}\begin{bmatrix}\boldsymbol{i_{L\_matrix}}\\ \boldsymbol{v_{p\_matrix}}\\ \boldsymbol{v_{s\_matrix}}\end{bmatrix}\\ &+ \boldsymbol{Y_{matrix}}5 v_{\text{in}}\end{aligned} \tag{6}$$

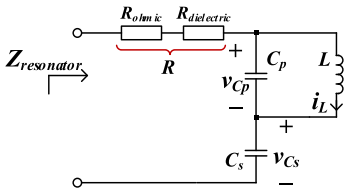

Fig. 11. Circuit model for separating dielectric loss and ohmic loss.

As Table IV shows, Design 1 shows the highest quality factor of 210.6 at its resonant frequency of 11.64 MHz, while Designs 2 and 3 achieve the quality factors of 177.5 and 56.2, respectively. Although the equivalent inductances L of the three designs are similar, the equivalent capacitances C_s and C_p vary significantly, with Design 3 featuring the largest capacitance. These differences reflect the properties of the three dielectric materials particularly in the middle layer. Air possesses the lowest dielectric constant and loss, while FR4 exhibits a relatively high dielectric constant and dielectric loss. Mica features high dielectric constant and low loss.

The equivalent capacitances C_s and C_p in Design 2 are only slightly higher than those in Design 1, which are still much lower than those in Design 3. This is attributed to imperfect contact between the middle dielectric layer and the spiral windings, as well as impurities within the mica sheets used for constructing Design 2. Table II summarizes the nominal and measured dielectric constant values for three different dielectric materials. The mica sheets used in Design 2 exhibit a measured dielectric constant of only 1.3, lower than their nominal value.

B. Characterization of Dielectric Loss

We characterize the dielectric loss by adapting the technique in [21]. This involves using full-wave finite-element simulation [34] to separate the total loss into its dielectric loss and ohmic loss, as shown in Fig. 11. The resonator impedance curves are obtained through adaptive frequency sweeping in finite-element simulations. The dielectric constant of the middle layer in Design 2 is set to the measured value of 1.30 to maintain consistency with the experiment.

In the first set of simulations, the dielectric material's loss tangent is set to its nominal value. Using a parameter extraction method [i.e., (4) and (5)], the circuit parameters, including the total resistance, can be derived from the simulated impedance curves. This total resistance R includes both dielectric loss and ohmic loss, i.e., $R = R_{\text{dielectric}}+R_{\text{ohmic}}$.

To separate these loss components, a second set of simulations is performed. In this case, the dielectric material's loss tangent is artificially set to zero, so the impedance curve only reflects the ohmic loss, i.e., $R = R_{\text{ohmic}}$. By comparing the results of the two simulation sets, $R_{\text{dielectric}}$ and R_{ohmic} are determined and summarized in Table V. The results indicate that the ohmic losses are similar in the three designs. However, Design 1 and Design 2 demonstrate a significant reduction (~80% reduction) in dielectric loss as compared with Design 3.

TABLE V
FINITE-ELEMENT CHARACTERIZATION OF DIELECTRIC LOSS

		Design 1	Design 2	Design 3
Loss tangent at nominal value	L (μH)	1.053	1.049	1.038
	C_s (pF)	121.6	143.3	421.5
	C_p (pF)	42.05	47.49	112.7
	Q	202.8	195.7	40.81
	$R_{dielectric}+R_{ohmic}$ (Ω)	0.7159	0.6715	1.735
Loss tangent=0	L (μH)	1.053	1.049	1.038
	C_s (pF)	121.6	143.3	421.5
	C_p (pF)	42.05	47.49	112.7
	Q	332.7	298.9	182.9
	R_{ohmic} (Ω)	0.4365	0.4397	0.3871
Summary	R_{ohmic} (Ω)	0.4365	0.4397	0.3871
	$R_{dielectric}$ (Ω)	0.2794	0.2318	1.3479

The bold entities are the headings of the rows and columns.

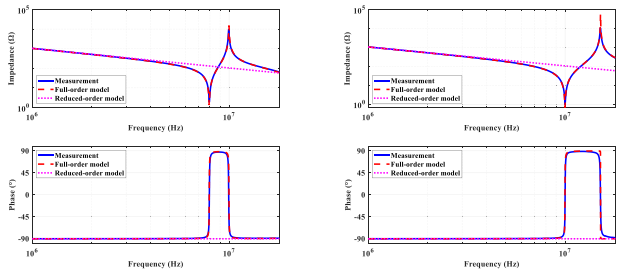

(a) (b)

Fig. 12. Input impedance curves of the coupled resonators of Design 1 with a distance of 2.5 mm along the z-axis. Amplitude and phase plots of the input impedance with (a) short-circuit load (i.e., $R_L = 0$) and (b) open-circuit load (i.e., $R_L = +\infty$).

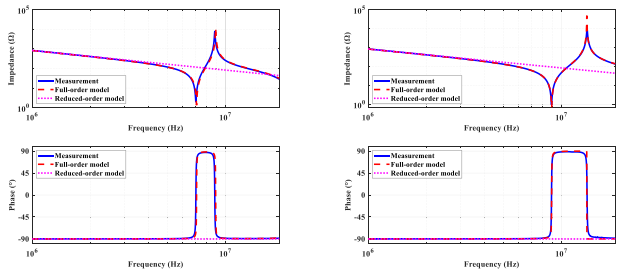

(a) (b)

Fig. 13. Input impedance curves of the coupled resonators of Design 2 with a distance of 2.5 mm along the z-axis. Amplitude and phase plots of the input impedance with (a) short-circuit load (i.e., $R_L = 0$) and (b) open-circuit load (i.e., $R_L = +\infty$).

C. Circuit Parameters for Hybrid Coupling

To investigate the hybrid coupling, the circuit parameters (e.g., mutual inductance M and mutual capacitance C_m) of the coupled resonators with different transmission distances are extracted. Figs. 12–14 show the input impedance curves of coupled DSL-PCB resonators with a transmission distance of 2.5 mm along the z-axis for Design 1, Design 2, and Design 3. These results show good agreement between the full-order model and practical measurements, validating the equivalent circuit model. The reduced-order model accurately characterizes

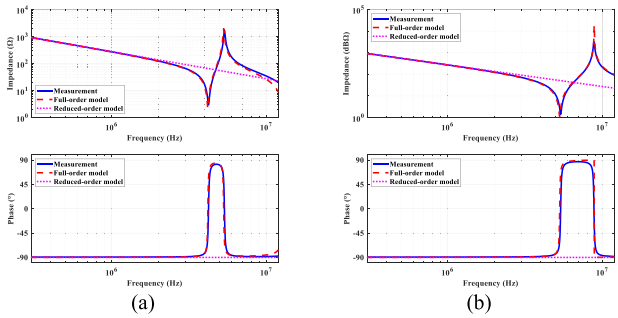

Fig. 14. Input impedance curves of the coupled resonators of Design 3 with a distance of 2.5 mm along the z-axis. Amplitude and phase plots of the input impedance with (a) short-circuit load (i.e., $R_L = 0$) and (b) open-circuit load (i.e., $R_L = +\infty$).

TABLE VI
CIRCUIT PARAMETERS OF COUPLED RESONATOR DESIGNS AT VARYING DISTANCES

Distance d_z	Circuit parameters	Design 1	Design 2	Design 3
2.5 mm	C_{sc} (pF)	153.3	193.5	578.5
	C_m (pF)	13.7	13.3	23.0
	C_{pc} (pF)	63.1	78.2	172.2
	M (μH)	−0.761	−0.785	−0.826
	R_m (Ω)	0.1000	0.0999	0.0999
6 mm	C_{sc} (pF)	140.1	178.1	572.2
	C_m (pF)	6.20	7.06	11.4
	C_{pc} (pF)	55.0	68.1	155.0
	M (μH)	−0.702	−0.701	−0.784
	R_m (Ω)	0.0998	0.1000	0.0998
10 mm	C_{sc} (pF)	138.7	173.8	569.9
	C_m (pF)	5.19	6.18	7.64
	C_{pc} (pF)	51.8	65.4	154.0
	M (μH)	−0.625	−0.615	−0.692
	R_m (Ω)	0.0994	0.0994	0.0998
25 mm	C_{sc} (pF)	136.3	170.6	568.4
	C_m (pF)	2.91	3.48	4.74
	C_{pc} (pF)	51.7	62.5	153.9
	M (μH)	−0.384	−4.06	−0.464
	R_m (Ω)	0.1000	0.0995	0.0997
50 mm	C_{sc} (pF)	137.3	170.5	568.2
	C_m (pF)	0.138	0.170	3.50
	C_{pc} (pF)	50.2	68.2	155.9
	M (μH)	−0.234	−0.243	−0.269
	R_m (Ω)	0.0993	0.0986	0.0998

The bold entities are the headings of the rows and columns.

the system impedance up to 3 MHz and the error becomes more obvious after 5 MHz.

D. Characterization of Hybrid Coupling Between Resonators With Varying Transmission Distances

By repeating the parameters extraction for a range of transmission distances along the z-axis (see Fig. 5), the corresponding circuit parameters are tabulated in Table VI. These results reflect the performance against vertical misalignment (along the z-axis). For the lawn mower charging application, horizontal misalignment (along the x- or y-axis) is minimized by the robot's charging station docking. Although the circular winding structure of DSL-PCB resonator is sensitive to horizontal misalignment, this is less of a concern in this application.

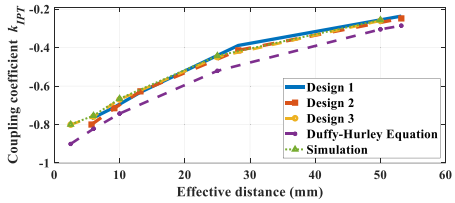

Fig. 15. Relationship of the mutual coupling k_{IPT} as a function of the effective distance.

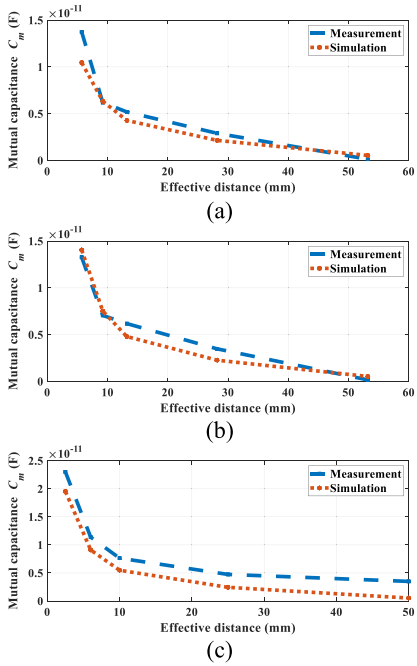

Fig. 16. Relationship of mutual capacitance as a function of effective distance. The results from the measurement and simulation of (a) Design 1, (b) Design 2, and (c) Design 3.

As Designs 1 and 2 involve DSL-PCB materials on top and bottom layers, the effective distance (i.e., the distance between the copper spiral windings of two resonators) is larger than that in Design 3 (of traditional DL-PCB). To ensure a fair comparison, we use the effective distance as a variable in studying the hybrid coupling. Fig. 15 shows the relationship of coupling coefficient k_{IPT} ($k_{\mathrm{IPT}} = M/L$) as a function of effective distance. The results obtained from Duffy–Hurley equation [22], [23], [35] are included for reference. In addition, since the inductive coupling mechanism of the three designs is identical, only the full-wave finite-element simulation of Design 3 is provided for reference. Notably, self-inductance and mutual inductance cannot be derived from the Duffy–Hurley equation, as it does not account for the effects of stray capacitance and self-resonance.

Fig. 16 shows the relationship of mutual capacitance C_m as a function of the effective distance. The simulation results,

obtained through electrostatic finite-element simulation, are provided for references. The simulation provides the capacitance of six coupling capacitors between two couplers. The mutual capacitance C_m is derived based on these six capacitor values [24], [25]. These results indicate that the experimental results and theoretical predictions are consistent.

E. Mixed Coupling Coefficient

The mixed coupling coefficient k_{mix} [36], [37], which accounts for both inductive and capacitive coupling, can be derived for DSL-PCB resonators. The procedure is provided in Appendix I. The mixed coupling coefficient k_{mix} is written as follows:

$$k_{\text{mix}} = \frac{k_{\text{IPT}} - k_{\text{CPT}}}{1 - k_{\text{CPT}} k_{\text{IPT}}} \tag{10}$$

where inductive coupling coefficient $k_{\text{IPT}} = \frac{M}{L}$ and capacitive coupling coefficient $k_{\text{CPT}} = \frac{C_m}{C_{pc}+C_{sc}}$.

Based on Table VI, $0 > k_{\text{IPT}} > -1$ and $1 > k_{\text{CPT}} > 0$. The mixed coupling coefficient is greater than the inductive coupling coefficient k_{IPT} and capacitive coupling coefficient k_{CPT}

$$\begin{aligned} &|k_{\text{mix}}| = \tfrac{|k_{\text{IPT}}|+|k_{\text{CPT}}|}{1+|k_{\text{CPT}}||k_{\text{IPT}}|} > \tfrac{|k_{\text{IPT}}|+|k_{\text{IPT}}|^2|k_{\text{CPT}}|}{1+|k_{\text{CPT}}||k_{\text{IPT}}|} = |k_{\text{IPT}}| \\ &\text{and} \\ &|k_{\text{mix}}| = \tfrac{|k_{\text{IPT}}|+|k_{\text{CPT}}|}{1+|k_{\text{CPT}}||k_{\text{IPT}}|} > \tfrac{|k_{\text{CPT}}|+|k_{\text{CPT}}|^2|k_{\text{IPT}}|}{1+|k_{\text{CPT}}||k_{\text{IPT}}|} = |k_{\text{CPT}}|\,. \end{aligned} \tag{11}$$

The sign of the coupling coefficient is critical. If k_{IPT} is positive, k_{IPT} and k_{CPT} will cancel out each other and weaken k_{mix}. From a circuit perspective, a positive k_{IPT} indicates that the transmission power through the inductive and capacitive coupling paths is in the opposite directions. This leads to a circulating power and extra conduction loss.

Fig. 17 illustrates the relationship between the coupling coefficient and effective distance. At a short distance, the capacitive coupling k_{CPT} is strong; the mixed coupling k_{mix} shows an improvement over inductive coupling k_{IPT}. As the distance increases, the capacitive coupling k_{CPT} reduces. Therefore, the mixed coupling k_{mix} gradually decreases to the inductive coupling k_{IPT} value.

F. General kQ *Factor and Optimal Transmission Efficiency*

Conventional kQ factor for inductive coupler is not suitable for characterizing DSL-PCB resonators because of the hybrid coupling mechanism. To address this, we use the general kQ factor [38], which is applicable to various types of couplers. The derivation of the general kQ factor for DSL-PCB resonators is detailed in Appendix II. The general kQ factor of the coupled DSL-PCB resonators kQ_{Hybrid} can be expressed as follows:

$$kQ_{\text{Hybrid}} = \underbrace{\frac{1}{|1-\omega^2 C_{pc}(L+M)|\,|1-\omega^2 C_{pc}(L-M)|}\frac{\omega|M|}{R}}_{\text{Contribution of inductive coupling, } kQ_{\text{IPT}}} + \underbrace{\frac{C_m}{\omega R\left(C_{sc}{}^2 - C_m{}^2\right)}}_{\text{Contribution of capacitive coupling, } kQ_{\text{CPT}}}. \tag{12}$$

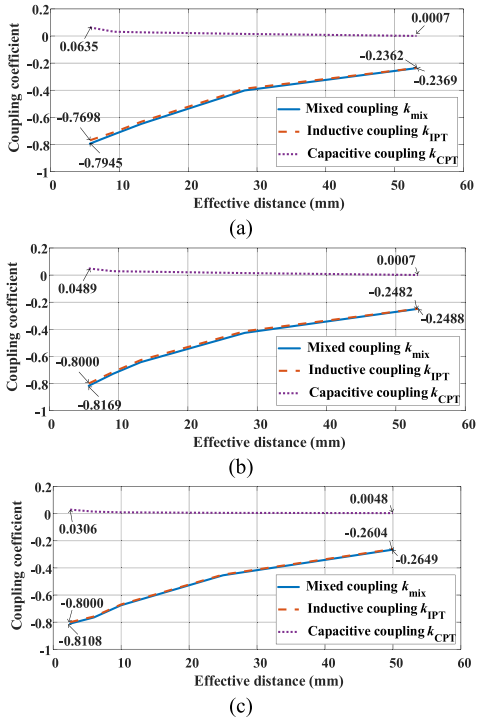

Fig. 17. Coupling coefficients as a function of effective distance. (a) Design 1. (b) Design 2. (c) Design 3.

The kQ factor of the coupled DSL-PCB resonators kQ_{Hybrid} is improved by two factors: First, the self-resonant operation amplifies that of the inductive coupling ($kQ_{\text{IPT}} > \frac{\omega|M|}{R}$), and second, the additional contribution of kQ_{CPT}. Based on kQ_{Hybrid}, the optimal efficiency of DSL-PCB resonators can be derived [39]

$$\eta_{\max} = \frac{\left(kQ_{\text{Hybrid}}\right)^2}{\left(1+\sqrt{1+\left(kQ_{\text{Hybrid}}\right)^2}\right)^2}. \tag{13}$$

Fig. 18 shows the relationship between kQ factors and effective distance, while Fig. 19 shows the optimal efficiency of three designs as a function of effective distance.

G. Pareto Front of Transmission Efficiency and Power

This study examines the tradeoff between transmission efficiency and power by presenting the Pareto fronts of three designs at different transmission distances. The Pareto fronts of three designs are obtained by solving a multiobjective optimization problem. The genetic algorithm is used for solver

$$\begin{aligned} &\min_{f,R_L} \begin{cases} -P_o(f,R_L) \\ -\eta(f,R_L) \end{cases} \\ &\text{s.t.} \begin{cases} f_{\min} \le f \le f_{\max} \\ R_{L\_\min} \le R_L \le R_{L\_\max}. \end{cases} \end{aligned} \tag{14}$$

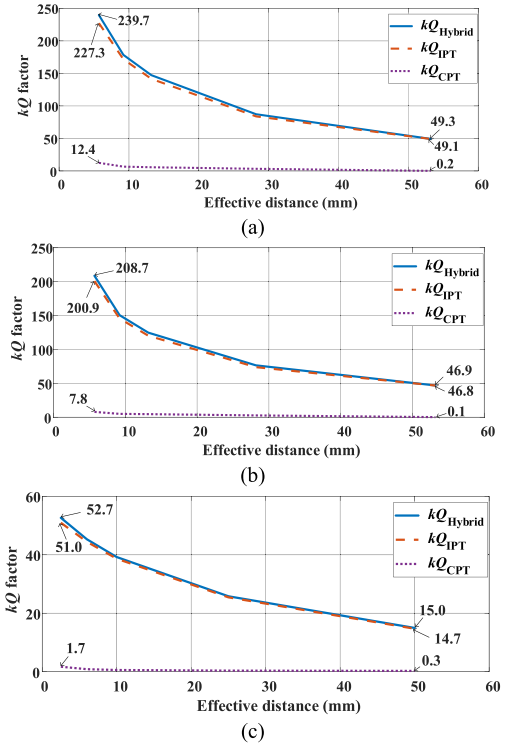

Fig. 18. kQ factors as a function of effective distance. (a) Design 1. (b) Design 2. (c) Design 3.

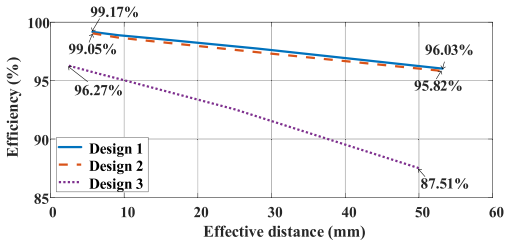

Fig. 19. Optimal transmission efficiency of three designs.

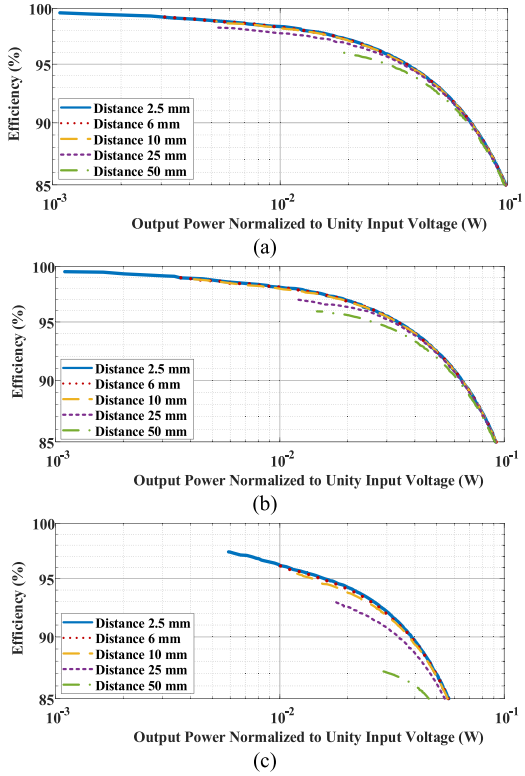

Fig. 20. Pareto fronts of three designs at different transmission distances. (a) Design 1. (b) Design 2. (c) Design 3.

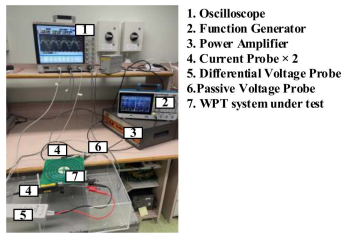

Fig. 21. Experimental setup for testing the DSL-PCB resonators.

The output power P_o and efficiency η are obtained through numerical calculation in Appendix III. The output power is normalized to the unity input voltage ($V_{\text{in}} = 1$ V). The minimum and maximum operating frequencies are set at $0.8f_r$–$1.2f_r$, respectively. The load resistance range is set to vary from 1–10^5 Ω.

Fig. 20 shows the Pareto fronts of three designs at different transmission distances. The data points located in the upper-left corner of each Pareto front correspond to the optimal transmission efficiencies of three designs. Conversely, the points in the lower right corner represent the maximum achievable output power when the minimum required transmission efficiency is set at 85% . Design 1, with a higher kQ factor, outperforms the other two designs by achieving higher optimal transmission efficiency and a wider output power range. Therefore, high-Q DSL-PCB resonator simultaneously improves efficiency and power performance, expanding the boundaries of the power–efficiency tradeoff.

V. Experimental Results

The experimental setup for verifying the WPT system with two coupled DSL-PCB resonators is shown in Fig. 21. A 75A250A power amplifier and an AFG31000 signal generator are used to generate a high-frequency ac power source. The following instruments are used for practical measurements: one 500 MHz DSOS054A oscilloscope, two 100 MHz N2783B current probes, one 100 MHz N2790A differential voltage probe, and one 500 MHz N2873A passive voltage probe. These instruments are used to measure the voltage and current waveforms of the WPT system. The ground terminal of the passive voltage probe is connected to the ground of the power amplifier, establishing a common ground connection among the oscilloscope, signal generator, and power amplifier, which alleviates the common-mode interference. Moreover, to ensure more accurate measurements, these probes are calibrated using the U1880A Deskew Fixture [40].

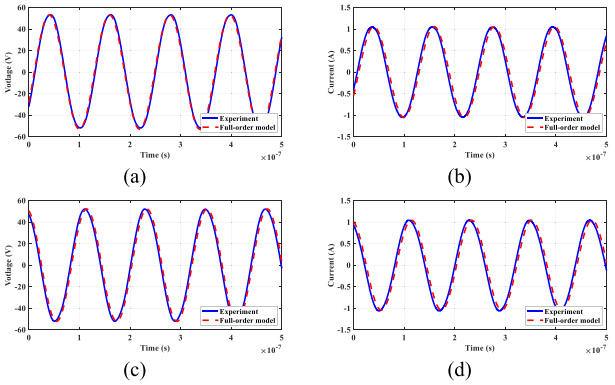

Fig. 22. Key waveforms of the WPT system with Design 1. (a) Input voltage. (b) Input current. (c) Output voltage. (d) Output current.

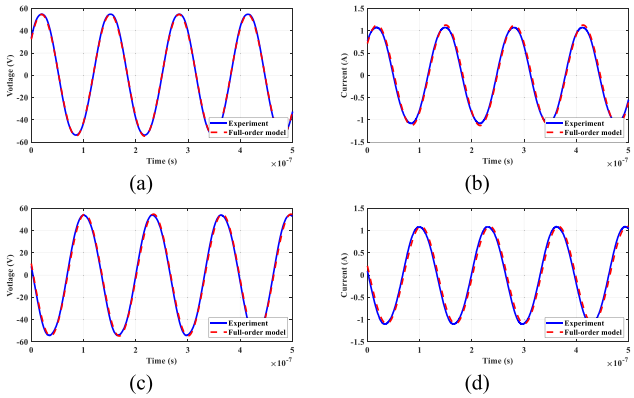

Fig. 23. Key waveforms of the WPT system with Design 2. (a) Input voltage. (b) Input current. (c) Output voltage. (d) Output current.

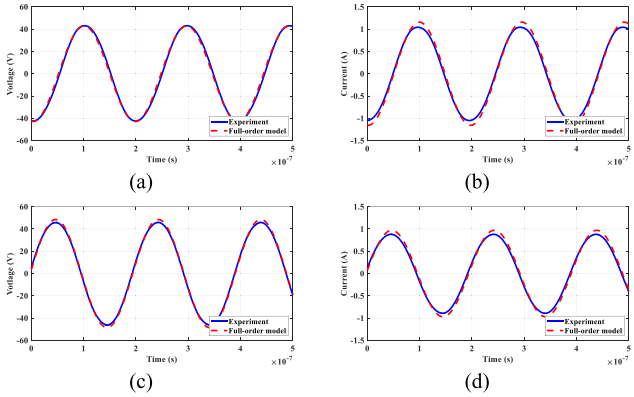

Fig. 24. Key waveforms of the WPT system with Design 3. (a) Input voltage. (b) Input current. (c) Output voltage. (d) Output current.

A. Model Verifications and Loss Analysis

Figs. 22–24 present the time-domain measurements and corresponding simulated waveforms obtained from the full-order circuit model. The coupled resonators are separated by 2.5 mm, and a 50-Ω load resistance is used. The operating frequencies for these three designs are 8.4 MHz, 7.6 MHz, and 5.1 MHz, respectively. These frequencies are close to the parity-time symmetry frequencies [41], resulting in an input impedance near 50 Ω as seen from the transmitter. This impedance matches that of the power amplifier, which allows effective power generation from the power amplifier. The measurement data closely match the results from the full-order circuit model, validating the model's effectiveness.

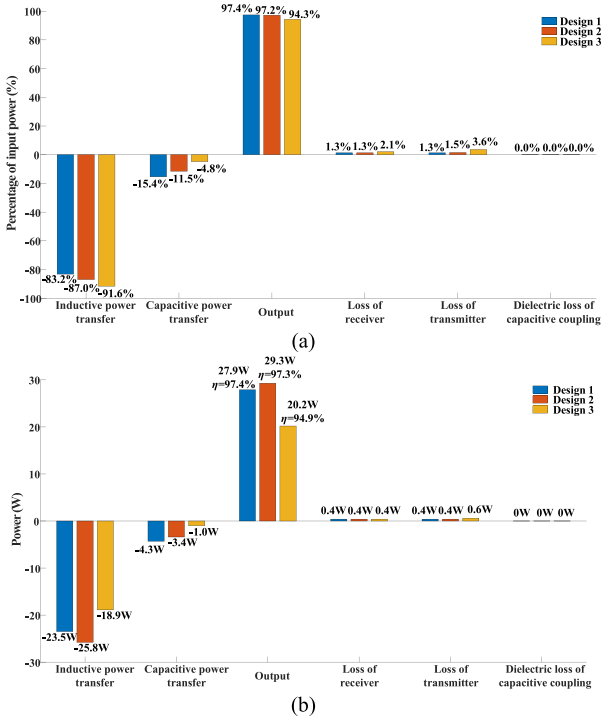

Fig. 25. Power flow analysis and loss breakdown of the WPT systems. (a) Estimated loss breakdown. (b) Power flow analysis.

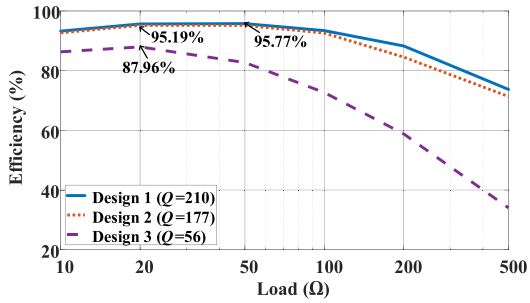

Fig. 26. Efficiency comparison of three designs under varying load conditions at a distance of 50 mm.

The circuit model enables an analysis of power flow. This analysis characterizes the power distribution through the two distinct coupling paths. Fig. 25(a) and (b) presents the estimated loss breakdowns and power flow analysis, respectively. The loss breakdown in Fig. 25(a) is estimated based on the model. In the power flow analysis, as shown in Fig. 25(b), the output power, efficiency, and loss are derived from waveforms, and the power of the IPT and CPT paths is estimated based on the

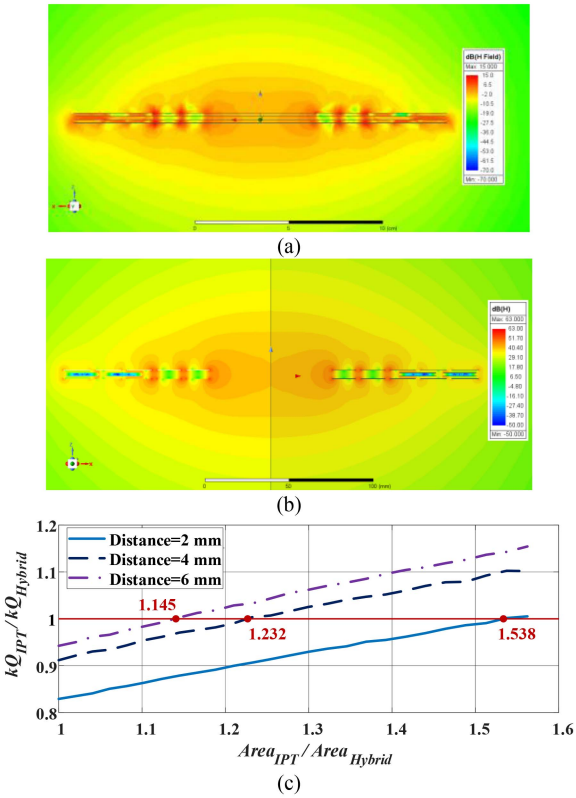

Fig. 27. Comparative study to quantify the extra area required by the inductive coupler. (a) Full-wave finite-element analysis for DSL-PCB resonator. (b) Quasistatic finite-element analysis for inductive coupler. (c) Additional area required by inductive couplers to achieve equivalent performance with DSL-PCB resonators.

model. Fig. 25(b) shows that the WPT system based on Design 1 achieves the highest transmission efficiency of 97.4% at 27.9 W output power. Design 2 exhibits a similarly high efficiency of 97.3% at 29.3 W output power. Design 3 shows a slightly lower efficiency of 94.9% at 20.2 W. In Fig. 25(a), the loss breakdown indicates the contribution of the capacitive coupling path, which transfers an additional 15% of power, as evidenced by the results from Design 1. These findings further validate the effectiveness of hybrid inductive and capacitive WPT.

B. Efficiency Comparison

In the experiment, we use high-bandwidth current probes and a high-resolution oscilloscope to obtain the root-mean-square values of i_{in} and i_o. The efficiency is then determined using (21). Similar measurement methods have been previously employed to determine ac power [42] and efficiency [43] in MHz-range WPT systems.

Fig. 26 presents the efficiency of three WPT system designs under varying load conditions at a distance of 50 mm. The systems operate at the resonators' respective self-resonant frequencies: 11.64, 10.50, and 5.85 MHz. The maximum efficiencies achieved by the three designs are 95.8%, 95.2%, and 88.0%, respectively. These results are consistent with the optimal efficiency prediction in Fig. 19. Design 3 consistently demonstrated lower efficiency than the other two designs, and this efficiency decreased substantially with higher load resistances. The observed trend is consistent with the resonator quality factors, with Design 3 possessing the lowest quality factor.

These tests verify that DSL-PCB resonators are suitable for both short- and long-distance wireless power transmission applications.

VI. Comparison

A. Comparison of Coupler Area

This section presents a comparative analysis designed to determine the additional area required by inductive couplers to achieve equivalent performance with DSL-PCB resonators. The kQ factor is used as the performance indicator.

Consequently, an inductive coupler with the spiral winding parameters, as listed in Table I, is used for comparison with the DSL-PCB resonator. Therefore, the size of inductive coupler is 200 mm $\times$ 200 mm. Quasistatic finite-element solver is carried out to evaluate the inductive coupler to minimize the effects of stray capacitance and dielectric loss at MHz frequencies. For consistency, the dielectric materials of the DSL-PCB resonators are excluded in the full-wave finite-element solver. In the comparative study, the operating frequency is set at 11.64 MHz.

Given an identical coupler area (i.e., the DSL-PCB resonator area $\text{Area}_{\text{Hybrid}}$ equals the inductive coupler area Area_{IPT}), kQ_{Hybrid} is generally greater than kQ_{IPT}. Increasing the inductive coupler area Area_{IPT} results in improved kQ_{IPT}. This enables the identification of critical inductive coupler area where $kQ_{\text{IPT}} = kQ_{\text{Hybrid}}$. Fig. 27(a) and (b) shows the finite-element analysis for the comparative study. Fig. 27(c) shows the relationship between the ratios $\frac{kQ_{\text{IPT}}}{kQ_{\text{Hybrid}}}$ and $\frac{\text{Area}_{\text{IPT}}}{\text{Area}_{\text{Hybrid}}}$ for three transmission distances. The data show that the inductive coupler requires a larger area increase at shorter distances to achieve an identical kQ factor. For example, at the transmission distance of 2 mm, the area needs to increase by approximately 53.8% (from 200 mm $\times$ 200 mm to 248 mm $\times$ 248 mm), while at the transmission distance of 6 mm, the additional area is only about 14.5% (from 200 mm $\times$ 200 mm to 214 mm $\times$ 214 mm). This is consistent with the previous analysis. At larger transmission distances, capacitive coupling diminishes, and the performance of the hybrid coupler becomes similar to that of the inductive coupler.

B. Comparison With Couplers From Literature

The comparison of various couplers is shown in Table VII. The kQ factor, mixed coupling coefficient, and optimal efficiency are also used as a performance indicator. As these resonators have different dimensions, the performance indicators are evaluated at a distance corresponding to a specific ratio of their sizes. The distance is set at 2.85% of the length. This distance corresponds to the smallest effective distances for characterizing the hybrid coupling in Figs. 15 and 16. The coupling coefficients

TABLE VII
COMPARISON BETWEEN INDUCTIVE AND CAPACITIVE COUPLERS

		[19]	[21]	[24]	[25]	[26]	[27]	**This work (Design 1)**
Information from the literature	**Shape and size**	Circular, Diameter: 200 mm	Circular, Diameter: 210 mm	Square, 120 mm × 200 mm × 2 (plates)	Square, 914 mm × 914 mm	Square, 300 mm × 300 mm	Square, 600 mm × 600 mm	**Circular, Diameter: 200 mm**
	Structure of the couplers	Monolithic planar PCB windings	Monolithic planar PCB windings	PCB metallic plates	Aluminum plates	Aluminum plates and coils	Aluminum plates and coils	**Monolithic planar PCB windings**
	Coupling mechanism	Inductive	Inductive	Capacitive	Capacitive	Hybrid	Hybrid	**Hybrid**
	Magnetic core	No	No	N.A.	N.A.	Ferrite	No	**No**
	Compensation	Self-resonance	Self-resonance	External LCL circuit and capacitor	External LCL circuit	Self-compensation	Partial self-compensation and external capacitor	**Self-resonance**
	Resonant /operating frequency	1.11 MHz	2.961 MHz	2 MHz	1 MHz	0.728–1.188 MHz	1 MHz	**11.64 MHz**
	***Q* Factor**	132	198.6	343	N.A.	N.A.	N.A.	**210.6**
	Transmission distance	1.14 m	300 mm	10–80 mm	150 mm	10 mm	60 mm	**2.5–50 mm**
	Maximum power	20 W	5 W	45 W	1.88 kW	626 W	707 W	**27.9 W**
	Maximum Efficiency	46% (Transmission efficiency for multi-coil system)	87.3% (Transmission efficiency for multi-coil system)	95% (Transmission efficiency) 88% (System efficiency)	85.87% (System efficiency)	95.7% (System efficiency)	88.3% (System efficiency)	**97.4% (Transmission efficiency)**
Performance evaluation at the specified distance	**Coupling coefficient**	0.8336	0.8036	0.9397*, 0.1440**	0.1298	CPT: 0.0319 IPT: 0.3214† 0.8823††	CPT: 0.5507* 0.1626** IPT: 0.4801	**0.7945**
	***kQ* factor**	110.04	159.59	322.32*, 49.39**	N.A.	N.A.	N.A.	**239.5**
	Optimal efficiency	98.20%	98.75%	99.38%*, 96.03**	N.A.	N.A.	N.A.	**99.17%**

*CPT coupler without compensation capacitors
**CPT coupler with compensation capacitors
†Coil without ferrite
††Coil with ferrite
The bold entities are the headings of the rows and columns.

for the inductive couplers are derived from the Duffy–Hurley equation [22], while the coupling coefficient for the capacitive coupler is obtained from finite-element analysis. However, the coupling coefficients of the hybrid couplers are obtained from finite-element analysis. The quality factors of these resonators are extracted from the literature.

In Table VII, the inductive couplers [19], [21], capacitive couplers [24], [25], and hybrid couplers with self- or partial self-compensation [26], [27] are included. The operating principles of these hybrid couplers are different from those of DSL-PCB resonators. These hybrid couplers [26], [27] employ electrically connected metallic plates (CPT coupler) and coils (IPT) for hybrid coupling and self-compensation, resulting in separated inductive (coil based) and capacitive (metallic plate based) coupling. DSL-PCB resonators, however, feature a monolithic structure without such electrical connections. Instead, the inherent stray capacitance and PCB windings interact to create self-resonance, which alters the current and voltage distribution within the resonator. In turn, the electric and magnetic field distributions are influenced. This results in a strong interdependence among inductive coupling, capacitive coupling, and self-resonant operation.

By comparing the data reported in the literature with the evaluated performance indicators, the DSL-PCB resonators demonstrate outstanding performance in enhancing the coupling coefficient, *kQ* factor, and optimal efficiency.

VII. CONCLUSION

This article presents a new wide-frequency equivalent circuit model for DSL-PCB resonators, based on which a WPT system comprising two DSL-PCB resonators is formed. Procedures for extracting the model parameters for both the resonators and WPT system are introduced. The DSL-PCB resonator circuit model and the corresponding WPT system model are verified in the MHz range experimentally. The first key advantage of the DSL-PCB resonators is the elimination of the dielectric power loss in the middle layer of the resonator. Its second advantage is

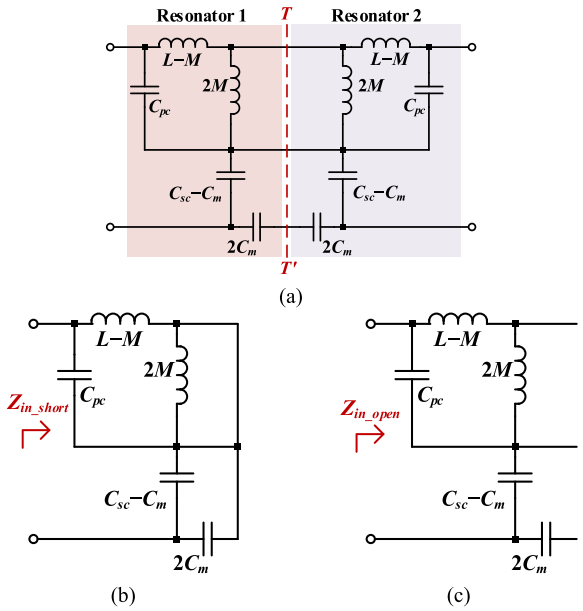

Fig. 28. (a) Alternative form of the circuit model. T–T' represents the symmetry plane for the circuit. (b) Left half of the circuit after replacing the symmetry plane with a short circuit. (c) Left half of the circuit after replacing the symmetry plane with an open circuit.

the reduction of both interwinding capacitance and intrawinding capacitance of the PCB resonators. Consequently, WPT systems based on DSL-PCB resonators can be operated in the MHz with high energy efficiency as practically proven in this study. A third advantage is that they allow both inductive and capacitive WPT. Finally, because the DSL-PCB resonators can be manufactured with relatively tight parameter tolerance using modern printing technology, they are suitable for mass production for WPT applications in the MHz range.

Appendix I
Derivation of Mixed Coupling Coefficient

A mixed coupling coefficient k_{mix} is derived following the procedure in [36] and [37]. The equivalent circuit for a pair of coupled DSL-PCB resonators can be transformed into an alternative form by using impedance inverter for inductive coupling and admittance inverter for capacitive coupling. Fig. 28(a) shows the alternative form of the circuit model. The equivalent resistors are hidden to simplify the derivation. The line T–T' represents the symmetry plane for the circuit. By replacing the symmetry plane with a short circuit, the left and right halves of the circuit are decoupled, as shown in Fig. 28(b). The resonance frequency f_{short} of the left-half part is

$$f_{\text{short}} = \frac{1}{2\pi\sqrt{(L-M)\left(C_{pc}+C_{sc}+C_m\right)}}. \tag{15}$$

Likewise, by replacing the symmetry plane with an open circuit, the left and right halves of the circuit are separated, as shown in Fig. 28(c). The resonance frequency f_{open} of the left-half part is

$$f_{\text{open}} = \frac{1}{2\pi\sqrt{(L+M)\left(C_{pc}+C_{sc}-C_m\right)}}. \tag{16}$$

The mixed coupling can be derived as

$$k_{\text{mix}} = \frac{{f_{\text{short}}}^2 - {f_{\text{open}}}^2}{{f_{\text{short}}}^2 + {f_{\text{open}}}^2} = \frac{\frac{M}{L} - \frac{C_m}{C_{pc}+C_{sc}}}{1 - \frac{M}{L}\frac{C_m}{C_{pc}+C_{sc}}} = \frac{k_{\text{IPT}} - k_{\text{CPT}}}{1 - k_{\text{CPT}}k_{\text{IPT}}}. \tag{17}$$

Appendix II
Derivation of the General kQ Factor

The general kQ factor [38] is used to characterize the hybrid coupling between two DSL-PCB resonators, which is defined as

$$kQ = \frac{|Z_{21}|}{\sqrt{\text{real}\left(Z_{11}\right)\text{real}\left(Z_{22}\right) - \text{real}\left(Z_{12}\right)\text{real}\left(Z_{21}\right)}}. \tag{18}$$

Based on the circuit model [in Fig. 9(a)], the real parts of Z_{11} and Z_{22} are

$$\text{real}\left(Z_{11}\right) = \text{real}\left(Z_{22}\right) = R. \tag{19}$$

Since the circuit model in Fig. 9(a) is reciprocal, Z_{21} and Z_{12} are identical. As the loss on R_m is negligible, the real part of Z_{21} and Z_{12} can be assumed to be zero, and hence, Z_{21} becomes a pure imaginary number. Z_{21} can be derived from the input impedance of the equivalent circuits in Fig. 28(b) and (c) [36]

$$\begin{aligned} Z_{21} = Z_{12} &= \frac{Z_{\text{in}_{\text{open}}} - Z_{\text{in}_{\text{short}}}}{2} \\ &= \frac{1}{2}\left[\frac{j\omega\left(L+M\right)}{1-\omega^2 C_{pc}\left(L+M\right)} - \frac{j\omega\left(L-M\right)}{1-\omega^2 C_{pc}\left(L-M\right)}\right] \\ &\quad + \frac{1}{2}\left[\frac{1}{j\omega\left(C_{sc}-C_m\right)} - \frac{1}{j\omega\left(C_{sc}+C_m\right)}\right] \\ &= \frac{j\omega M}{\left[1-\omega^2 C_{pc}\left(L+M\right)\right]\left[1-\omega^2 C_{pc}\left(L-M\right)\right]} \\ &\quad - j\frac{C_m}{\omega\left({C_{sc}}^2 - {C_m}^2\right)}. \end{aligned} \tag{20}$$

The kQ factor is

$$kQ = \frac{1}{\left|1-\omega^2 C_{pc}\left(L+M\right)\right|\left|1-\omega^2 C_{pc}\left(L-M\right)\right|}\frac{\omega|M|}{R} + \frac{C_m}{\omega R\left({C_{sc}}^2 - {C_m}^2\right)}. \tag{21}$$

APPENDIX III
OUTPUT POWER AND EFFICIENCY OF THE COUPLED DSL-PCB RESONATORS

The circuit model of coupled resonators is of seventh order; it is not straightforward to derive a closed-form analytical expression for efficiency and output power calculation. Therefore, we use numerical methods to determine efficiency in time domain and frequency domain.

A. Time-Domain Calculation

Since the loss associated with R_m is small enough to be considered negligible [see Fig. 25(a)], the output power and efficiency of the WPT system can be simplified as (22) shown at the bottom of this page,where P_o is the output power, P_{loss} is the loss, $T(=1/f)$ is the period of sinusoidal input $v_{\text{in}} = V_{\text{in}}\sin(2\pi ft)$, τ is the starting time for efficiency calculation, and n is a positive natural number. By solving the differential equations [see (6)] of the coupled DSL-PCB resonators, the values of $i_{\text{in}}(t)$ and $i_o(t)$ are obtained. To increase the accuracy of efficiency calculation, a sufficiently large τ is used such that the WPT system is operating at steady state. Power is calculated over n cycles to reduce the effects of noise.

B. Frequency-Domain Calculation

Moreover, the output power and efficiency can be numerically determined in the frequency domain. The Z parameters for the coupled DSL-PCB resonators are derived from the input impedance of the equivalent circuits, as shown in Fig. 28(b) and (c) [36]. The Z parameters are expressed as follows:

$$\begin{aligned} Z_{11} = Z_{22} &= \frac{Z_{\text{in\_open}} + Z_{\text{in\_short}}}{2} + R \\ &= \frac{1}{2}\left[\frac{j\omega(L+M)}{1-\omega^2 C_{pc}(L+M)} + \frac{j\omega(L-M)}{1-\omega^2 C_{pc}(L-M)}\right] \\ &\quad + \frac{1}{2}\left[\frac{1}{j\omega(C_{sc}-C_m)} + \frac{1}{j\omega(C_{sc}+C_m)}\right] + R \\ &= \frac{j\left[\omega L - \omega^3 C_{pc}(L+M)(L-M)\right]}{\left[1-\omega^2 C_{pc}(L+M)\right]\left[1-\omega^2 C_{pc}(L-M)\right]} \\ &\quad - j\frac{C_{sc}}{\omega\left({C_{sc}}^2 - {C_m}^2\right)} + R \\ Z_{21} = Z_{12} &= \frac{Z_{\text{in\_open}} - Z_{\text{in\_short}}}{2} \\ &= \frac{j\omega M}{\left[1-\omega^2 C_{pc}(L+M)\right]\left[1-\omega^2 C_{pc}(L-M)\right]} \\ &\quad - j\frac{C_m}{\omega\left({C_{sc}}^2 - {C_m}^2\right)}. \end{aligned} \tag{23}$$

The input and output current are obtained by solving the matrix inversion

$$\begin{aligned} \begin{bmatrix} i_{\text{in}} \\ i_o \end{bmatrix} &= \begin{bmatrix} Z_{11} & Z_{12} \\ Z_{21} & Z_{22}+R_L \end{bmatrix}^{-1} \begin{bmatrix} V_{\text{in}} \\ 0 \end{bmatrix} \\ &= \begin{bmatrix} \frac{(Z_{22}+R_L)V_{\text{in}}}{Z_{11}(Z_{22}+R_L)-Z_{12}Z_{21}} \\ \frac{-Z_{21}V_{\text{in}}}{Z_{11}(Z_{22}+R_L)-Z_{12}Z_{21}} \end{bmatrix}. \end{aligned} \tag{24}$$

Through substituting the circuit parameters, the output power and efficiency are numerically obtained

$$\begin{aligned} P_o &= \frac{1}{2}|i_o|^2 R_L = \frac{|Z_{21}|^2 |V_{\text{in}}|^2 R_L}{2\left|Z_{11}(Z_{22}+R_L) - Z_{12}Z_{21}\right|^2} \\ \eta &= \frac{|i_o|^2 R_L}{|i_o|^2(R_L+R) + |i_{\text{in}}|^2 R} \\ &= \frac{|Z_{21}|^2 R_L}{|Z_{21}|^2(R_L+R) + |Z_{22}+R_L|^2 R}. \end{aligned} \tag{25}$$

REFERENCES

[1] K. Li, J. Wu, S. C. Tan, and S. Y. R. Hui, "Design and modelling of a mega-hertz PCB resonator with hybrid inductive and capacitive wireless power transfer capability," in *Proc. IEEE Energy Convers. Congr. Expo.*, 2024, pp. 7100–7104.

[2] A. Ghahary and B. H. Cho, "Design of a transcutaneous energy transmission systems using a series resonant converter," in *Proc. 21st Annu. IEEE Conf. Power Electron. Specialists*, 1990, pp. 1–8.

[3] A. W. Green and J. T. Boys, "10 kHz inductively coupled power transfer-concept and control," in *Proc. 5th Int. Conf. Power Electron. Variable-Speed Drives*, 1994, pp. 694–699.

[4] S. Y. R. Hui and S. C. Tang, "Coreless printed circuit board transformers," U.S. Patent 7 768 371, Feb. 1998.

[5] B. Choi, J. Nho, H. Cha, T. Ahn, and S. Choi, "Design and implementation of low-profile contactless battery charger using planar printed circuit board windings as energy transfer device," *IEEE Trans. Ind. Electron.*, vol. 51, no. 1, pp. 140–147, Feb. 2004.

[6] S. Y. R. Hui and W. C. Ho, "A new generation of universal contactless battery charging platform for portable consumer electronic equipment," *IEEE Trans. Power Electron.*, vol. 20, no. 3, pp. 620–627, May 2005.

[7] Wireless Power Consortium Website, 2024. [Online]. Available: https://www.wirelesspowerconsortium.com/22

[8] Fortune Business Insights Website: Wireless Charging Market, 2024. [Online]. Available: https://www.fortunebusinessinsights.com/wireless-charging-market-105183

[9] S. Y. R. Hui, "Magnetic resonance for wireless power transfer [a look back]," *IEEE Power Electron. Mag.*, vol. 3, no. 1, pp. 14–31, Mar. 2016.

[10] S. Y. R. Hui, W. Zhong, and C. K. Lee, "A critical review of recent progress in mid-range wireless power transfer," *IEEE Trans. Power Electron.*, vol. 29, no. 9, pp. 4500–4511, Sep. 2014.

[11] N. Tesla, *On Light and Other High Frequency Phenomena*. London, U.K.: DigiCat, 1893.

$$\begin{aligned} P_o &= \frac{1}{nT}\int_{\tau}^{\tau+nT}\left[i_o(t)\right]^2 R_L dt \\ \eta &= \frac{P_o}{P_o + P_{\text{loss}}} \approx \frac{\frac{1}{nT}\int_{\tau}^{\tau+nT}\left[i_o(t)\right]^2 R_L dt}{\frac{1}{nT}\int_{\tau}^{\tau+nT}\left[i_o(t)\right]^2 R_L dt + \frac{1}{nT}\int_{\tau}^{\tau+nT}\left[i_{\text{in}}(t)\right]^2 R dt + \frac{1}{nT}\int_{\tau}^{\tau+nT}\left[i_o(t)\right]^2 R dt} \end{aligned} \tag{22}$$

[12] S.-Y. R. Hui, Y. Yang, and C. Zhang, "Wireless power transfer: A paradigm shift for the next generation," *IEEE J. Emerg. Sel. Topics Power Electron.*, vol. 11, no. 3, pp. 2412–2427, Jun. 2023.
[13] K. Ogawa, K. Ozaki, M. Yamada, and K. Honda, "High efficiency small-sized rectenna using a high-Q LC resonator for long distance WPT at 950MHz," in *Proc. IEEE Int. Microw. Workshop Ser. Innov. Wireless Power Transmiss., Technol., Syst., Appl.*, 2012, pp. 255–258.
[14] R. S. Yang, A. J. Hanson, C. R. Sullivan, and D. J. Perreault, "Design flexibility of a modular low-loss high-frequency inductor structure," *IEEE Trans. Power Electron.*, vol. 36, no. 11, pp. 13013–13024, Nov. 2021.
[15] Z. Zhen et al., "Core energy capacitance of NiZn inductors," *IEEE Trans. Power Electron.*, vol. 38, no. 4, pp. 4235–4240, Apr. 2023.
[16] M. V. Joisher, R. S. Bayliss, M. K. Ranjram, R. S. Yang, A. Jurkov, and D. J. Perreault, "High-performance high-power inductor design for high-frequency applications," in *Proc. IEEE Appl. Power Electron. Conf. Expo.*, 2024, pp. 424–431.
[17] J. Qu, L. He, N. Tang, and C.-K. Lee, "Wireless power transfer using domino-resonator for 110-kV power grid online monitoring equipment," *IEEE Trans. Power Electron.*, vol. 35, no. 11, pp. 11380–11390, Nov. 2020.
[18] W. Zhou, P. Wu, W. C. Mu, W. Yu, and S. Y. Huang, "Compact broadband planar resonator with a viaed double spiral for robust wireless power transfer," *IEEE J. Electromagn., RF Microw. Med. Biol.*, vol. 5, no. 4, pp. 329–339, Dec. 2021.
[19] Y. Fang, J. Qu, B. M. H. Pong, C. K. Lee, and R. S. Y. Hui, "Quasi-static modeling and optimization of two-layer PCB resonators in wireless power transfer systems for 110kV power grid online monitoring equipment," *IEEE Trans. Ind. Electron.*, vol. 69, no. 2, pp. 1400–1410, Feb. 2022.
[20] K. Li and S. Y. R. Hui, "Printed circuit board resonator and method of forming the same," Int. Patent Appl. PCT/SG2024/050017, WO 2024/151212A1, 2024.
[21] K. Li, J. Wu, A. C. Yucel, and S.-Y. R. Hui, "New printed-circuit-board resonators with high quality factor and transmission efficiency for megahertz wireless power transfer applications," *IEEE Trans. Power Electron.*, vol. 38, no. 10, pp. 13207–13218, Oct. 2023.
[22] W. G. Hurley, M. C. Duffy, J. Zhang, I. Lope, B. Kunz, and W. H. Wölfle, "A unified approach to the calculation of self- and mutual-inductance for coaxial coils in air," *IEEE Trans. Power Electron.*, vol. 30, no. 11, pp. 6155–6162, Nov. 2015.
[23] W. G. Hurley and M. C. Duffy, "Calculation of self and mutual impedances in planar magnetic structures," *IEEE Trans. Magn.*, vol. 31, no. 4, pp. 2416–2422, Jul. 1995.
[24] S. Wang, J. Liang, and M. Fu, "Analysis and design of capacitive power transfer systems based on induced voltage source model," *IEEE Trans. Power Electron.*, vol. 35, no. 10, pp. 10532–10541, Oct. 2020.
[25] H. Zhang, F. Lu, H. Hofmann, W. Liu, and C. C. Mi, "A four-plate compact capacitive coupler design and LCL-compensated topology for capacitive power transfer in electric vehicle charging application," *IEEE Trans. Power Electron.*, vol. 31, no. 12, pp. 8541–8551, Dec. 2016.
[26] F. Wang, Q. Yang, X. Zhang, T. Chen, and G. Li, "Enhancing misalignment tolerance in hybrid wireless power transfer system with integrated coupler via frequency tuning," *IEEE Trans. Power Electron.*, vol. 39, no. 9, pp. 11885–11899, Sep. 2024.
[27] B. Luo, T. Long, L. Guo, R. Dai, R. Mai, and Z. He, "Analysis and design of inductive and capacitive hybrid wireless power transfer system for railway application," *IEEE Trans. Ind. Appl.*, vol. 56, no. 3, pp. 3034–3042, May/Jun. 2020.
[28] F. Lu, H. Zhang, H. Hofmann, and C. C. Mi, "An inductive and capacitive integrated coupler and its LCL compensation circuit design for wireless power transfer," *IEEE Trans. Ind. Appl.*, vol. 53, no. 5, pp. 4903–4913, Sep./Oct. 2017.
[29] Y. Wang, Z. Sun, X. Zhang, Y. Yang, and S. Y. R. Hui, "Integrated hybrid inductive and capacitive power transfer system with asymmetrical PCB self-resonator," in *Proc. IEEE Appl. Power Electron. Conf. Expo.*, 2025, pp. 3275–3280.
[30] Y. Wang, J. Yang, K. Wang, and Y. Yang, "Highly integrated hybrid inductive and capacitive power transfer system with asymmetrical printed-circuit-board-based self-resonator," *IEEE Trans. Power Electron.*, vol. 40, no. 7, pp. 10254–10264, Jul. 2025.
[31] S. Y. R. Hui and S. C. Tan, "Wireless charging system and docking station for mobile robots and light electric vehicles," U.S. Provisional Patent 63/772308, Mar. 2025.
[32] T. Hirano, "Relationship between Q factor and complex resonant frequency: Investigations using RLC series circuit," *IEICE Electron. Exp.*, vol. 14, no. 21, Nov. 2017, Art. no. 20170941.
[33] J. Schindler, "PT-symmetric electronics," M.A. dissertation, Dept. Phys., Wesleyan Univ., Middletown, CT, USA, 2013.
[34] "RF module user's guide," COMSOL, 2023. [Online]. Available: https://doc.comsol.com/6.2/doc/com.comsol.help.rf/RFModuleUsersGuide.pdf
[35] J. Wu, K. Li, S.-C. Tan, and S.-Y. R. Hui, "Optimized design and performance analysis of 13.56 MHz printed-circuit-board resonators for efficient wireless power transfer," in *Proc. IEEE Wireless Power Technol. Conf. Expo.*, 2024, pp. 271–274.
[36] J.-S. Hong and M. J. Lancaster, "Couplings of microstrip square open-loop resonators for cross-coupled planar microwave filters," *IEEE Trans. Microw. Theory Techn.*, vol. 44, no. 11, pp. 2099–2109, Nov. 1996.
[37] J.-S. Hong and M. J. Lancaster, *Microstrip Filters for RF/Microwave Applications*. Hoboken, NJ, USA: Wiley, 2001.
[38] T. Ohira, "The kQ product as viewed by an analog circuit engineer," *IEEE Circuits Syst. Mag.*, vol. 17, no. 1, pp. 27–32, Jan./Mar. 2017.
[39] T. Ohira, "Power transfer theory on linear passive two-port systems," *IEICE Trans. Electron.*, vol. 101, no. 10, pp. 719–726, Oct. 2018.
[40] Keysight Technol., "U1880A deskew fixture user's guide," 2008. [Online]. Available: https://www.keysight.com/hk/en/assets/9018-01957/user-manuals/9018-01957.pdf
[41] J. Zhou, B. Zhang, W. Xiao, D. Qiu, and Y. Chen, "Nonlinear parity-time-symmetric model for constant efficiency wireless power transfer: Application to a drone-in-flight wireless charging platform," *IEEE Trans. Ind. Electron.*, vol. 66, no. 5, pp. 4097–4107, May 2019.
[42] J. Choi, D. Tsukiyama, Y. Tsuruda, and J. M. R. Davila, "High-frequency, high-power resonant inverter with eGaN FET for wireless power transfer," *IEEE Trans. Power Electron.*, vol. 33, no. 3, pp. 1890–1896, Mar. 2018.
[43] A. Kurs et al., "Wireless power transfer via strongly coupled magnetic resonances," *Science*, vol. 31, pp. 83–86, Jul. 2017.

Kerui Li (Member, IEEE) received the B.Eng. degree from the South China University of Technology, Guangzhou, China, in 2013, the M.Eng. degree from Sun Yat-sen University, Guangzhou, China, in 2016, and the Ph.D. degree from The University of Hong Kong, Hong Kong, in 2021.

He is currently a Research Assistant Professor with the Department of Electrical Engineering, The City University of Hong Kong, Hong Kong. His research interests include wireless power transfer and power electronics.

Dr. Li was a recipient of several prestigious awards, including two IEEE Transactions on Power Electronics Prize Paper Awards (second place in 2024 and first place in 2023), for his research, the IEEE Power Electronics Society Ph.D. Thesis Talk Award in 2022, and the University of Hong Kong Power Engineering Prize in 2020.

Jiayang Wu (Member, IEEE) received the B.Eng. degree in electrical information engineering from Zhejiang University, Hangzhou, China, in 2017, and the Ph.D. degree in electrical and electronic engineering from The University of Hong Kong, Hong Kong, in 2022.

She was a Research Fellow with the School of Electrical and Electronic Engineering, Nanyang Technological University, Singapore, in 2023. Following this role, she held the position of a Research Assistant Professor with the Department of Electrical and Electronic Engineering, The University of Hong Kong, Hong Kong, in 2024. She is currently a Research Assistant Professor with the Department of Electrical Engineering, City University of Hong Kong. Her current research interests include wireless power transfer, electric vehicle charging, resonant converters, and renewable energy.

Dr. Wu was a recipient of the Best Paper Award (Second Place) of the IEEE TRANSACTIONS ON POWER ELECTRONICS in 2019 and 2023, and the Best Presentation Award of the IEEE Applied Power Electronics Conference and Exposition in 2024. She also holds two Chinese patents and one U.S. patent.

Siew-Chong Tan (Fellow, IEEE) received the B.Eng.(Hons.) and M.Eng. degrees in electrical and computer engineering from the National University of Singapore, Singapore, in 2000 and 2002, respectively, and the Ph.D. degree in electronic and information engineering from The Hong Kong Polytechnic University, Hong Kong, in 2005.

He is currently a Chair Professor with the Department of Electrical Engineering, City University of Hong Kong, Hong Kong. He was a Visiting Scholar with the Grainger Center for Electric Machinery and Electromechanics, University of Illinois at Urbana-Champaign, Champaign, from September to October 2009, and an Invited Academic Visitor of the Huazhong University of Science and Technology, Wuhan, China, in December 2011. His research interests are focused in the areas of power electronics and control, LED lightings, smart grids, and clean energy technologies.

Ka Wai Eric Cheng (Fellow, IEEE) received the B.Sc. degree in electrical and electronic engineering and the Ph.D. degree in power electronics from the University of Bath, Bath, U.K., in 1987 and 1990, respectively.

Prior to joining The Hong Kong Polytechnic University in 1997, he served as a Principal Engineer with Lucas Aerospace, U.K. He is currently a Professor of electrical engineering with the School of Engineering, University of California, Merced, CA, USA. He has authored or coauthored more than 500 articles and 7 books. His research spans power electronics, motor drives, electromagnetic interference, electric vehicles, battery management, and energy saving.

Dr. Cheng was a recipient of the IEE Sebastian Z De Ferranti Premium Award in 1995, followed by the Outstanding Consultancy Award in 2000, and the Faculty Merit Award for Best Teaching in 2003 and the Faculty Engineering Industrial and Engineering Services Grant Achievement Award in 2006, honored by The Hong Kong Polytechnic University. His innovative work earned him the Brussels Innova Energy Gold Medal with Mention in 2007, the Consumer Product Design Award in 2008, and the Electric Vehicle Team Merit Award in 2009. Subsequent recognitions include the Eco Star Award in 2012, the Gold Prize at the Seoul International Invention Fair in 2015, and the iCAN Gold Medal in Canada in 2016 for his contributions to active suspension systems. More recently, he was awarded the Hong Kong Innovation and Technology Gold Award in 2017 for developing vehicle-integrated supercapacitor technology, the Geneva Invention Expo Silver Medal in 2021 for e-Antilock Braking Systems, and both the TechConnect 2023 and Geneva Invention 2024 awards for his groundbreaking work on Ammonia-Powered Electric Vehicles.

Shu-Yuen Ron Hui (Fellow, IEEE) received the B.Sc.(Eng.)(Hons.) degree in electrical and electronic engineering from the University of Birmingham, Birmingham, U.K., in 1984, and the D.I.C. and Ph.D. degrees in electrical engineering from Imperial College London, London, U.K., in 1987.

He is currently the Chair Professor of power electronics with the City University of Hong Kong, Hong Kong, and Imperial College London. Previously, he held academic positions with the University of Nottingham and University of Sydney, and endowed professorship with the University of Hong Kong. He has authored or coauthored more than 500 research papers, including 330 refereed journal publications. His IEEE Xplore patent citations exceed 1280. Over 150 of his patents have been adopted by industry worldwide. His research interests include power electronics, wireless power, sustainable lighting, and smart grid. His inventions on wireless charging platform technology underpin key dimensions of Qi, the world's first wireless power standard, with freedom of positioning and localized charging features for wireless charging of consumer electronics. He also developed the Photo-Electro-Thermal Theory for LED Systems and Electric Spring technology for smart grid.

Dr. Hui was a recipient of the IEEE Rudolf Chope R&D Award and the IET Achievement Medal (The Crompton Medal) in 2010, the IEEE William E. Newell Power Electronics Award in 2015, and the IET JJ Thomson Medal in 2024. He is a Fellow of the Australian Academy of Technology and Engineering, U.S. National Academy of Inventors, and Royal Academy of Engineering, U.K.